CHAPTER 4

Molecular Thermodynamic Models for Fluids of Chain-Like Molecules, Applications in Phase Equilibria and Micro-Phase Separation in Bulk and at Interface

Honglai Liu, Ying Hu, Xueqian Chen, Xingqing Xiao and **Yongmin Huang**

Contents

State Key Laboratory of Chemical Engineering and Department of Chemistry, East China University of Science and Technology, Shanghai 200237, China

Advances in Chemical Engineering, Volume 40
ISSN 0065-2377, DOI 10.1016/B978-0-12-380985-8.00004-X

Abstract

Molecular thermodynamic models based on lattice framework have been widely applied to study the thermodynamic properties and the phase behaviors of chain-like fluids. Recently, we have developed a new molecular thermodynamic model by combining statistical mechanics theory with computer simulation. The effects of branching, coordination number, chain stiffness, composition, hydrogen bonding and pressure on thermodynamic properties and phase behaviors can be well described by the new model. Satisfactory agreement is obtained between the predicted results and Monte Carlo (MC) simulation data for multicomponent Ising and Flory–Huggins lattice systems. The model can be used to satisfactorily correlate phase equilibria including vapor–liquid and liquid–liquid equilibria for the mixtures of ordinary fluids, polymers, and ionic liquids. Incorporated with density functional theory (DFT) for nonuniform fluids and weighted-density approximation (WDA), the model can also be used to describe the adsorption of polymer at solid–liquid interface and conformation distributions at interfacial regions. For the morphologies of micro-phase separation of diblock copolymers confined in curved surfaces, a framework has been developed based on the strong segregation limit (SSL) theory. The SSL predictions agree well with simulation and experimental results on multilayer transitions. Upon comparison between theoretical predictions and MC simulations, we have established a numerical calculation method of the Helmholtz energy for a special structure called the complex multilayered sector column (CMSC)

structure. Finally, the detailed theoretical studies together with simulations indicate that the CMSC structure tends to be formed at higher thickness, while the mutually competing concentric cylinder barrel and the sector column structures appear at lower thickness.

1. INTRODUCTION

A large number of new functional materials used in engineering practice have unique meso-scale structures related to the processes over a wide range of length and time scales. These meso-scale structures determine the properties of functional materials. To design and control material manufacturing, it is crucial to understand the formation mechanisms of the meso-scale structures and to investigate the effects of different engineering factors such as the changes of flow field, temperature gradient, and external field on the structures. For example, copolymers typically with multi-scale structures can be used as templates to prepare various complex materials (Bates, 1991; Park *et al*., 1997; Xia *et al*., 1999; Li and Huck, 2002). To realize the regulation of the meso-scale structures of copolymer materials, there are three fundamental questions. What are the physical conditions for microphase separation to form materials with desired compositions and meso-scale structures in different domains? How are the meso-scale structures evolved during preparation period? What is the composition or density profile at interface, which might determine the stability and properties of the material? The first question can be solved by an equilibrium thermodynamic theory (e.g., an equation of state (EOS) or a Helmholtz energy model)(Prausnitz *et al*., 1999), or by computer simulation such as Monte Carlo (MC) and molecular dynamics (MD) (Sadus, 1999). The second question involves the dynamics of meso-structure evolution that can be examined by field-based theories (e.g., time-dependent Ginzburg–Landau equation (TDGL)(Chaikin and Lubensky, 1995), self-consistent-field theory (SCFT)(Matsen and Barrett, 1998), dynamic density functional theory (DDFT)(Fraaije, 1993), and the cell dynamics system method (CDS))(Oono and Shiwa, 1987; Oono and Puri, 1988), or by coarse-graining simulations (e.g., dissipative particle dynamics (DPD)(Groot and Warren, 1997), kinetic Monte Carlo (KMC)(Graham and Olmsted, 2010), Langevin dynamics (LD) (Pankavich *et al*., 2009), and lattice Boltzmann (LB) method) (Song *et al*., 2008). The last question can be addressed by density functional theory (DFT)(Wu, 2006) and SCFT (Scheutjens and Fleer, 1979), also by simulations (Chen *et al*., 2010; Feng *et al*., 2005).

In our laboratory, we have developed a multi-scale theory to study above questions based on an off-lattice model for polymer materials (Liu *et al*., 2008). We first developed a molecular thermodynamic model (EOS and Helmholtz energy model) for square-well fluids (SWCF-EOS) based on the statistical mechanics theory of association. Combining SWCF-EOS with the Langevin equation and adopting a weighted-density approximation (WDA), we then developed a DDFT based on equation of state (EOS-based DDFT). Finally, this SWCF-EOS with WDA was applied for polymers at interfaces. The key of the theory is the development of the EOS or Helmholtz energy model for homogeneous fluid at a molecular level. The molecular parameters in model can be obtained by the regression of experimental vapor pressure and/or *pVT* data of pure substance. This EOS or Helmholtz energy model can be used to accurately describe vapor–liquid equilibria (VLE), liquid–liquid equilibria (LLE), and solid–liquid equilibria (SLE) for nonpolar, polar, and associating small molecules, as well as polymers and ionic liquids (Hu *et al*., 1996a; Liu and Hu, 1998; Peng *et al*., 2001; Peng *et al*., 2002; Peng *et al*., 2003; Li *et al*., 2009a; Li *et al*., 2009b; Li *et al*., 2009c). The EOS-based DDFT can describe the meso-scale structures of polymers and their evolution dynamics. The effect of pressure on meso-phase separation can be successfully predicted (Xu *et al*., 2007a; Xu *et al*., 2007b; Xu *et al*., 2008a). DFT could describe the density distribution and molecular conformation of polymer at interface (Cai *et al*., 2002; Zhang *et al*., 2004; Ye *et al*., 2005; Ye *et al*., 2006; Chen *et al*., 2006a; Ye *et al*., 2007; Chen *et al*., 2007; Chen *et al*., 2008).

In this review, we introduce another approach to study the multi-scale structures of polymer materials based on a lattice model. We first show the development of a Helmholtz energy model of mixing for polymers based on close-packed lattice model by combining molecular simulation with statistical mechanics. Then, holes are introduced to account for the effect of pressure. Combined with WDA, this model of Helmholtz energy is further applied to develop a new lattice DFT to calculate the adsorption of polymers at solid–liquid interface. Finally, we develop a framework based on the strong segregation limit (SSL) theory to predict the morphologies of micro-phase separation of diblock copolymers confined in curved surfaces.

2. LATTICE BASED MOLECULAR THERMODYNAMIC MODEL OF POLYMER SYSTEMS

In a lattice model, molecules are assumed to be arranged regularly on an array of sites or cells as shown in Figures 1 and 2, each polymer chain

consists of r segments that occupy a series of r successive sites, each solvent molecule has one segment. A polymer system contains N_r simple cubic lattice sites, each site can be occupied by one segment of polymer or a solvent molecule. In close-packed lattice, there is no empty site as shown in Figure 1 corresponding to an incompressible polymer solution. There are interaction energies between nearest-neighbor segment-pair symbolized as $-\varepsilon$. If the segment numbers of all molecules are equal to 1, it is the Ising lattice. For realistic lattice fluids, in addition to the segments of polymer and solvent molecules, there are vacancies as shown in Figure 2 corresponding to a compressible polymer solution.

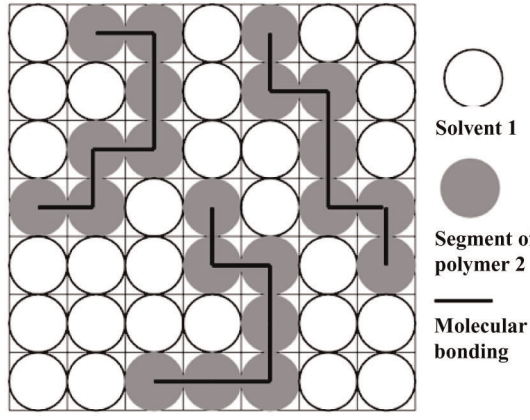

Figure 1 Close-packed lattice model.

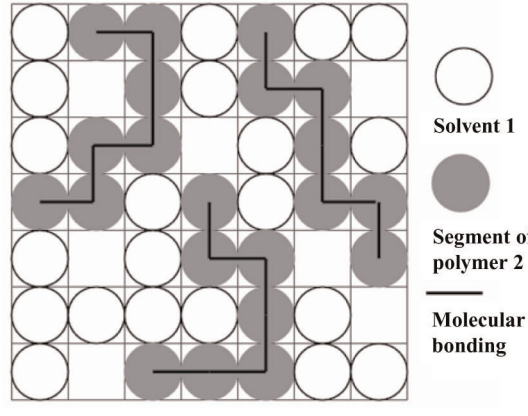

Figure 2 Lattice fluid model.

The number of vacancies is related to the pressure of the polymer system.

People have recognized the problems associated with lattice models over half a century. The most prominent one is that it is difficult to obtain concise and accurate analytical expressions for Helmholtz energy of mixing and other thermodynamic properties. Even for the simplest Ising lattice, only the one-dimensional (1D) and two-dimensional (2D) lattice can be rigorously solved on the basis of statistical mechanics. The three-dimensional (3D) lattice has yielded so far to rigorous analysis only by way of series expansion (Hill, 1956). An alternative way other than traditional statistical mechanical derivation might be needed. Toward this end, introducing molecular simulation into statistical mechanics to establish models seems to be useful (Hu and Liu, 2006). In off-lattice approaches, a good example is the well-known Carnahan–Starling equation for hard-sphere fluids (Carnahan and Starling, 1969). The equation was established by a linear combination of the PY pressure equation and compressibility equation; the coefficients were judged by simulation results. The EOS for hard-sphere chain fluids developed in our laboratory is another example (Hu *et al.*, 1996a). Based on the sticky-point model of Cummings, Zhou, and Stell (Cummings and Stell, 1984; Stell and Zhou, 1989; Zhou and Stell, 1992), an expression of residual Helmholtz energy in terms of cavity correlation function (CCF) was established where the nearest-neighbor CCF was derived from rigorous Tildesley–Streett equation (Tildesley and Streett, 1980) inducted from simulation of hard dumbbells, the next-to-nearest-neighbor CCF was obtained by fitting simulation of trimers. A concise EOS similar to the Carnahan–Starling equation was finally obtained for hard-sphere chain fluids. To develop the Helmholtz energy model of mixing for polymer systems based on lattice, we adopted the similar approach, that is, combining molecular simulation with statistical mechanics.

A wide variety of theories have been developed for polymer solutions over the later half of the last century. Among them, lattice model is still a convenient starting point. The most widely used and best known is the Flory–Huggins lattice theory (Flory, 1941; Huggins, 1941) based on a mean-field approach. However, it is known that a mean-field approximation cannot correctly describe the coexistence curves near the critical point (Fisher, 1967; Heller, 1967; Sengers and Sengers, 1978). The lattice cluster theory (LCT) developed by Freed and coworkers (Freed, 1985; Pesci and Freed, 1989; Madden *et al.*, 1990; Dudowicz and Freed, 1990; Dudowicz *et al.*, 1990; Dudowicz and Freed, 1992) in 1990s was a landmark.

Similar to Mayer's theory for nonideal gases, they developed a double expansion in power series with respect to the reciprocals of coordination number z and temperature T. However, because of the complexity of the expansion, lengthy equations are involved even for truncation at the first order or at the second order, its practical usage is largely limited. For some cases, the results are unsatisfactory, for example, the predicted critical compositions of binary polymer solutions exhibit unrealistic kink in contradictory with simulation (Madden *et al.*, 1990; Yan *et al.*, 1996; Panagiotopoulos and Wong, 1998). Also the predictions do not match well with simulated for ternary polymer systems (Jiang *et al.*, 1997). Hu et al. (Hu *et al.*, 1991a; Hu *et al.*, 1991b; Hu *et al.*, 1996b) developed a revised Freed Theory (RFT) by using an effective chain-insertion probability for entropy and a series expansion for energy. The former is used to improve the mean-field Flory–Huggins entropy term, while the latter is adopted to account for interactions between more than two segments. The coefficients in the model are determined by a few simulation data and referred to as a rigorous LCT. The agreement with simulation for spinodals and binodals is excellent, much better than the classical Flory–Huggins theory. The comparisons with calculated binodals and critical coordinates by LCT for binary and ternary systems over a wide range of chain lengths indicate that the two theories give almost same results. Lambert et al. (Lambert *et al.*, 1993) and Bae et al. (Chang *et al.*, 1998) have made similar improvements. Chen et al. (Chen *et al.*, 2000; Chen *et al.*, 2005) extended RFT to random copolymer solutions, Bae et al. (Chang and Bae, 2003; Oh and Bae, 2010a) extend their model to polymer blend systems.

Recently, we developed a new close-packed lattice model for polymer systems (Yang *et al.*, 2006a; Yang *et al.*, 2006b; Xin *et al.*, 2008a) based on Zhou–Stell theory (Stell and Zhou, 1989; Zhou and Stell, 1992). This model was extended to random copolymer systems (Xin *et al.*, 2008b) and used to develop an EOS based on lattice fluid model (Xu *et al.*, 2008b; Xu *et al.*, 2009a).

2.1 General framework

We start from a simple cubic lattice system containing N_r sites with a coordination number $z = 6$. The lattice is filled with K components of chain molecules. N_i and r_i are the number of molecules and chain length of component i, respectively. $r_i = 1$ means that the ith component is a solvent. The total number of lattice sites is $N_r = \sum_{i=1}^{K} N_i r_i$. Only the nearest-neighbor interactions are considered.

According to Gibbs–Helmholtz relationship, the Helmholtz energy of mixing of system can be obtained by integrating the internal energy

of mixing against the reciprocal of temperature:

$$\Delta_{\mathrm{mix}}F/T = (\Delta_{\mathrm{mix}}F/T)_{1/T\to 0} + \int_0^{1/T} (\Delta_{\mathrm{mix}}U)\mathrm{d}(1/T) \tag{1}$$

$(\Delta_{\mathrm{mix}}F/T)_{1/T\to 0}$ is the Helmholtz energy of mixing of system at temperature approaching to infinity. The interactions between segments have no effect on the thermodynamic properties at infinite temperature, $(\Delta_{\mathrm{mix}}F/T)_{1/T\to 0}$ is the negative of the athermal entropy of mixing $-\Delta_{\mathrm{mix}}S_0$. The second term on the right-hand side of Equation (1) is the residual contribution of the Helmholtz energy of mixing (ΔF^{r}) due to the interactions between segments that include the internal energy of mixing and the entropy arose from the interactions between segments. Equation (1) can be further expressed as

$$\Delta_{\mathrm{mix}}F = -T\Delta_{\mathrm{mix}}S_0 + \Delta F^r \tag{2}$$

To obtain the residual Helmholtz energy of mixing ΔF^{r}, we design a three-step process as shown in Figure 3 (Xin *et al.*, 2008c): (1) dissociate the pure chains to form pure monomers; (2) mix monomers and solvent to form an Ising mixture; and (3) associate the monomers into chain molecules. The residual Helmholtz energy of mixing ΔF^{r} can be expressed as

$$\Delta F^r = \Delta F_1^r + \Delta F_2^r + \Delta F_3^r \tag{3}$$

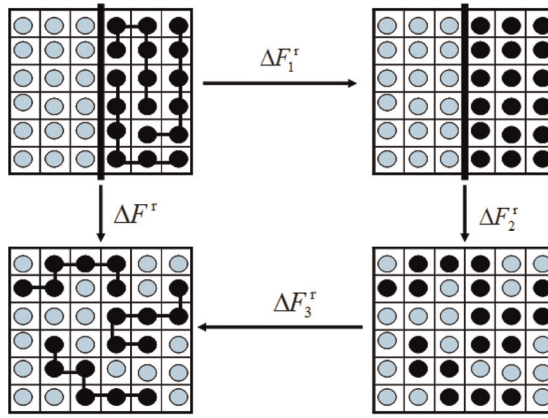

Figure 3 Sketch for the mixing process of chain-like molecular systems (Xin *et al.*, 2008c).

The second term on the right-hand side of Equation (1) is the residual Helmholtz energy of mixing for an Ising mixture ($\Delta_{mix}F^{r}_{Ising}$). Its expression will be discussed below.

For the contributions of step (1) and step (3) to the residual Helmholtz energy of mixing ($\Delta F^{r}_{1} + \Delta F^{r}_{3}$), the bond energies involved in the dissociation step (1) and the association step (3) are mutual compensated; therefore, they need not be considered in this scheme. However, their environments in the dissociation step (1) and the association step (3) are different, the entropy changes arisen from the dissociation and association of polymer chains are then different. In the step (1), dissociation occurs in pure substance, the environment has no change before and after dissociation, the entropy change is thus zero. While in the step (3), the association of polymer chains occurs in mixtures, the monomer of Ising mixture should be first arranged in the same conformation of polymer solution then bonded into chain-like molecules, the entropy is arisen from this configuration change of the Ising mixture. The formalism of chemical association through the CCF y in our previous work (Hu *et al.*, 1996a) based on the sticky-point model of Cummings, Zhou, and Stell (Cummings and Stell, 1984; Stell and Zhou, 1989; Zhou and Stell, 1992) can be employed. The total residual Helmholtz energy of mixing in the step (1) and step (3) is given by (Yang *et al.*, 2006a; Xin *et al.*, 2008a)

$$\Delta F_1^r + \Delta F_3^r = -\sum_{i=1}^{K} kTN_i \ln g_i^{(r_i)} \tag{4}$$

where $g^{(r2)}$ is the r-particle correlation function.

Currently, it is formidable, if not impossible, to derive an explicit expression for $g^{(r2)}$ solely by statistical mechanics. In off-lattice space, Zhou and Stell (Zhou and Stell, 1992) adopted a linear approximation and simplified the r-particle CCF by using the nearest-neighbor two-particle CCF. In our previous work for hard-sphere chain fluids, besides the nearest-neighbor two-particle CCF, we used the next to nearest correlations determined by simulation (Hu *et al.*, 1996a). In this work, we follow the similar approach. If we adopt Kirkwood's superposition approximation, we can write $g^{(r2)} = (g^{(2)})^{r2-1}$, where $g^{(2)}$ is the radial distribution function. However, this approximation neglects the long-range correlations. We then introduce a parameter λ into the exponential to account for the long-range correlations beyond the close contact pair, $g^{(r_2)} = (g^{(2)})^{r_2-1+\lambda}$, where $g^{(2)}$ and λ are to be determined. Then, Equation (4), the contribution of dissociation and association of polymer chains ($\Delta_{mix}F^{r}_{Chain}$), is

rewritten as

$$\frac{\Delta_{\text{mix}}F^r_{\text{chain}}}{N_r kT} = \frac{\Delta F^r_1 + \Delta F^r_1}{N_r kT} = -\sum_{i=1}^{K} \frac{(r_i - 1 + \lambda_i)}{r_i} \phi_i \ln g_i^{(2)} \tag{5}$$

Finally, we have the expression for the Helmholtz function of mixing $\Delta_{\text{mix}}F$,

$$\frac{\Delta_{\text{mix}}F}{N_r kT} = -\frac{\Delta_{\text{mix}}S_0}{N_r k} + \frac{\Delta_{\text{mix}}F^r_{\text{Ising}}}{N_r kT} + \frac{\Delta_{\text{mix}}F^r_{\text{chain}}}{N_r kT} \tag{6}$$

2.2 Athermal entropy of mixing

Among various theories for the athermal entropy of mixing $\Delta_{\text{mix}}S_0$, Staverman and Guggenheim's athermal entropy of mixing (Guggenheim, 1952) is proved to be the best by comparison with simulation (Hu and Liu, 2006; Yang *et al.*, 2006a). As shown in Figure 4 for chemical potentials of an athermal binary mixture with $r_1 = 1$ and $r_2 = 4$, and in Figure 5 for the generalized plot for the probabilities of 1–1 pairs versus surface fraction for athermal binary mixtures of $r_1 = 1$ and various chain lengths r_2, the predictions from Staverman–Guggenheim's theory are perfect, and much better than that from the Flory–Huggins theory. Therefore, we adopt Staverman–Guggenheim's athermal entropy of mixing (Guggenheim, 1952) for $\Delta_{\text{mix}}S_0$,

$$-\frac{\Delta_{\text{mix}}S_0}{N_r k} = -\frac{\Delta_{\text{mix}}S_{\text{Guggenheim}}}{N_r k} = \sum_{i=1}^{K} \frac{\phi_i}{r_i} \ln \phi_i + \frac{z}{2} \sum_{i=1}^{K} \phi_i \frac{q_i}{r_i} \ln \frac{\theta_i}{\phi_i} \tag{7}$$

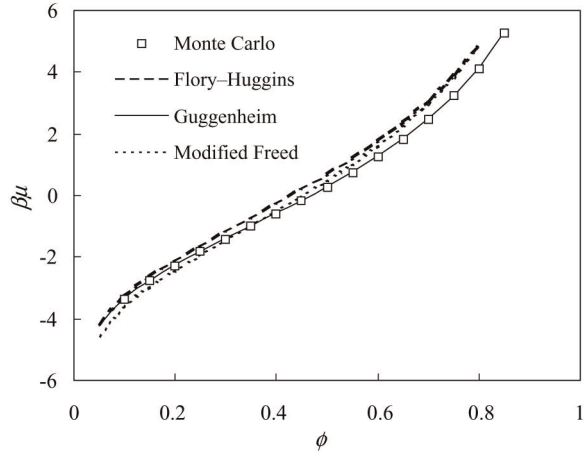

Figure 4 Chemical potentials of an athermal mixture with $r_2 = 4$.

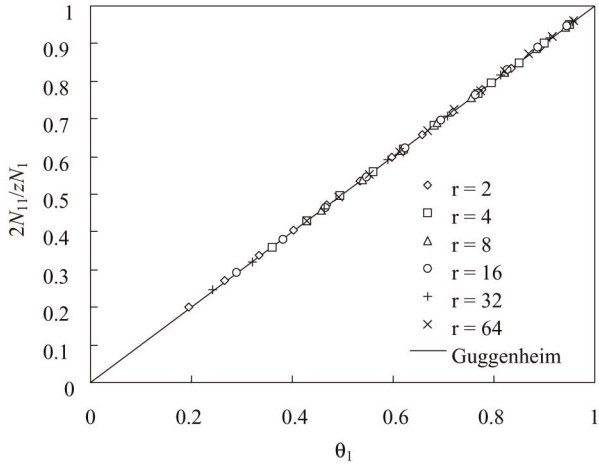

Figure 5 Probabilities of 1–1 pairs of athermal mixtures with different chain lengths (Yang *et al.*, 2006a).

where, z is the coordination number of the lattice. ϕ_i and θ_i are the volume fraction and surface fraction of component i, respectively, which can be calculated by $\phi_i = N_i r_i / \sum_{j=1}^{K} N_j r_j$ and $\theta_i = N_i q_i / \sum_{j=1}^{K} N_j q_j$, q_i is the surface area parameter defined as $q_i = [r_i(z-2)+2]/z$.

2.3 Residual Helmholtz energy of mixing for multicomponent Ising mixture

The Ising lattice is the simplest lattice model in which each molecule occupies a single site. Nevertheless, as mentioned above, due to mathematical difficulties, a rigorous analysis of the 3D Ising lattice has so far achieved only by means of series expansion (Hill, 1956). When the chain length is equal to 1, the Flory–Huggins theory and the Freed's LCT can also be used in Ising lattice (Hu *et al.*, 1991a; Hu *et al.*, 1991b; Hu *et al.*, 1996b). Other theories for the Ising lattice are Bragg–Williams approximation (Bragg and Williams, 1934), Bethe-approximation (Bethe and Wills, 1935), and Kikuchi's cluster variation method (Kikuchi, 1951), which have been employed to investigate the phase behavior of solid alloys. All these mean-field theories show comparable accuracy with the Flory–Huggins theory for the Ising lattice.

For a binary Ising lattice, we introduced a nonrandom factor that was observed from simulation to have a linear relation with composition. The characteristic parameter of the linear relation was found by combining a series expansion and the infinite dilution properties. On this basis, an accurate expression for the Helmholtz energy of mixing

was developed, which can accurately reproduce the critical point and coexistence curve of Ising lattice (Hu and Liu, 2006; Yan *et al.*, 2004). This model has been extended to multicomponent Ising mixture (Yang *et al.*, 2006ca). The predicted internal energy of mixing for ternary and quaternary systems match accurately with simulation results. The predicted liquid–liquid phase equilibria for ternary systems are in nearly perfect agreement with simulation results, and substantially improved against the Flory–Huggins theory and the LCT.

For a simple cubic Ising lattice with a total N_r sites is occupied by K types of molecules, each molecule occupies one site, the constrains $\sum_{i=1}^{K} N_i = N_r$ and $2N_{ii} + \sum_{j\neq i}^{K} N_{ij} = zN_i$ are satisfied, where N_i is the number of molecules of component i, N_{ij} is the number of i–j contact pairs, and $z = 6$ is the coordination number of the lattice. The internal energy of mixing of the Ising system can be calculated by

$$\Delta_{mix}U = \frac{1}{4}\sum_{i=1}^{K}\sum_{j=1}^{K} N_{ij}\in_{ij} \tag{8}$$

where $\in_{ij} = \varepsilon_{ii} + \varepsilon_{jj} - 2\varepsilon_{ij}$ is the exchange energy between components i and j. To calculate N_{ij}, a nonrandom factor f_{ij} is defined by $N_{ij}/2N_{ii} = f_{ij}x_j/x_i$, where $x_i = N_i/N_r$ is the mole fraction of component i. Then, we get the number of i–j contact pairs

$$N_{ij} = zN_r x_i x_j f_{ij} / \sum_{k=1}^{K} x_k f_{ik} \tag{9}$$

with $f_{ii} = 1$. By substituting Equation (9) into Equation (8), the internal energy of mixing is

$$\Delta_{mix}U = \frac{zN_r}{4}\sum_{i=1}^{K}\sum_{j=1}^{K} x_i x_j f_{ij}\in_{ij} / \sum_{k=1}^{K} x_k f_{ik} \tag{10}$$

The nonrandom factor f_{ij} characterizes the degree of deviation from ideal mixing, and its numerical value can be estimated directly by simulation. It is shown that $1/f_{ij}$ has a fairly well linear relation with mole fraction. For binary Ising lattice, the expression of f_{ij} was obtained by combining simulation and statistical mechanics (Yan *et al.*, 2004). For the multicomponent Ising lattice, a generalized expression has been proposed as

$$1/f_{ij} = \sum_{k=1}^{K} x_k \exp\left(\frac{\tilde{\varepsilon}_{ij} + \tilde{\varepsilon}_{ik} - \tilde{\varepsilon}_{jk}}{2}\right) \tag{11}$$

where $\tilde{\varepsilon}_{ij} = \beta\in_{ij}$ is the reduced exchange energy with $\beta = 1/kT$.

The Helmholtz energy of mixing can be obtained by substituting Equation (11) into Equation (10) and integrating Equation (10) with Gibbs–Helmholtz equation against the reciprocal of temperature. In the integration, we first expand it to a polynomial of the reciprocal of temperature for ternary Ising system ($K = 3$), then integrate and finally obtain the expression of Helmholtz energy of mixing by Gibbs–Helmholtz equation. The complete expression is very long and complicated even truncated at the third order of the reduced energy. For simplification and practical use, the expression is truncated at the second order of the temperature, with a constant c introduced to maintain accuracy. Finally, we have

$$\frac{\Delta_{\text{mix}}F}{N_r kT} = \sum_{i=1}^{K} x_i \ln x_i + \frac{z}{4}\sum_{i=1}^{K}\sum_{j=1}^{K} x_i x_j \tilde{\varepsilon}_{ij} - \frac{z}{16}\sum_{i=1}^{K}\sum_{j=1}^{K} x_i x_j \tilde{\varepsilon}_{ij}^2 + \frac{z}{8}\sum_{i=1}^{K}\sum_{j=1}^{K}\sum_{k=1}^{K} x_i x_j x_k \tilde{\varepsilon}_{ij}\tilde{\varepsilon}_{ik} - \frac{cz}{16}\left(\sum_{i=1}^{K}\sum_{j=1}^{K} x_i x_j \tilde{\varepsilon}_{ij}\right)^2 \tag{12}$$

By reproducing the critical point of binary Ising system, we get $c = 1.1$. Figure 6 shows the coexistence curves for binary Ising lattice predicted by this model, the Flory–Huggins model, and the Freed model. The predicted results of our model are in nearly perfect agreement with simulation data (Yan *et al.*, 1996). Figure 7 is the 3D diagram for the internal energy of mixing for a ternary Ising system with $\tilde{\varepsilon}_{12} = 0.4$, $\tilde{\varepsilon}_{13} = 0.3$, and $\tilde{\varepsilon}_{23} = 0.2$. All the simulation data (open squares) are distributed on the curved surface calculated by Equation (10).

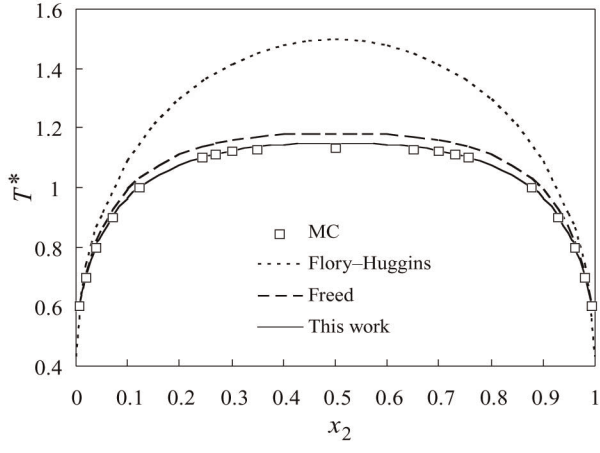

Figure 6 Coexistence curves of binary Ising lattice (Yan *et al.*, 2004).

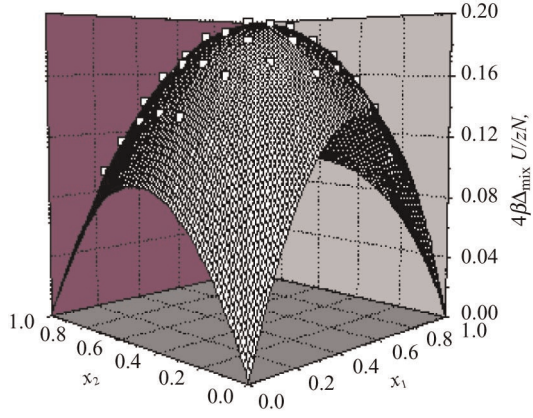

Figure 7 Internal energy of mixing for a ternary Ising lattice (Yang *et al.*, 2006ca).

By subtracting the Helmholtz energy of ideal mixing ($\sum_{i=1}^{K} x_i \ln x_i$), Equation (12) can be used to calculate the residual Helmholtz energy of mixing ($\Delta_{mix}F^{r}_{Ising}$) of monomer mixture of polymer system in step 2 of Figure 1. However, the mole fraction x_i should be replaced by volume fraction ϕ_i. We have

$$\frac{\Delta_{mix}F^{r}_{Ising}}{N_r kT} = \frac{z}{4}\sum_{i=1}^{K}\sum_{j=1}^{K}\phi_i\phi_j\tilde{\varepsilon}_{ij} - \frac{z}{16}\sum_{i=1}^{K}\sum_{j=1}^{K}\phi_i\phi_j\tilde{\varepsilon}_{ij}^2 + \frac{z}{8}\sum_{i=1}^{K}\sum_{j=1}^{K}\sum_{k=1}^{K}\phi_i\phi_j\phi_k\tilde{\varepsilon}_{ij}\tilde{\varepsilon}_{ik} - \frac{cz}{16}\left(\sum_{i=1}^{K}\sum_{j=1}^{K}\phi_i\phi_j\tilde{\varepsilon}_{ij}\right)^2 \quad (13)$$

2.4 The residual Helmholtz energy of dissociation and association of polymer chains

The residual Helmholtz energy due to the dissociation of polymer chains in pure state and the association of polymer chains in mixture state can be calculate by Equation (5). The pair correlation functions of component i in the corresponding Ising lattice system are calculated by $g_i^{(2)} = 1/\sum_{j=1}^{K}\phi_j f_{ij}$ (Liu *et al.*, 2007). The residual Helmholtz energy of dissociation and association of polymer chains is then

$$\frac{\Delta_{mix}F^{r}_{chain}}{N_r kT} = \sum_{i=1}^{K}\frac{(r_i - 1 + \lambda_i)}{r_i}\phi_i \ln\left(\sum_{j=1}^{K}\phi_j f_{ij}\right) \quad (14)$$

2.5 Helmholtz energy of mixing of polymer systems

Finally, by substituting Equations (7), (13), and (14) into Equation (7), we obtain the Helmholtz energy of mixing for multicomponent polymer systems

$$\frac{\Delta_{\text{mix}}F}{N_r kT} = \sum_{i=1}^{K}\frac{\phi_i}{r_i}\ln\phi_i + \frac{z}{2}\sum_{i=1}^{K}\phi_i\frac{q_i}{r_i}\ln\frac{\theta_i}{\phi_i} + \frac{z}{4}\sum_{i=1}^{K}\sum_{j=1}^{K}\phi_i\phi_j\tilde{\varepsilon}_{ij} - \frac{z}{16}\sum_{i=1}^{K}\sum_{j=1}^{K}\phi_i\phi_j\tilde{\varepsilon}_{ij}^2 + \frac{z}{8}\sum_{i=1}^{K}\sum_{j=1}^{K}\sum_{k=1}^{K}\phi_i\phi_j\phi_k\tilde{\varepsilon}_{ij}\tilde{\varepsilon}_{ik} - \frac{cz}{16}\left(\sum_{i=1}^{K}\sum_{j=1}^{K}\phi_i\phi_j\tilde{\varepsilon}_{ij}\right)^2 + \sum_{i=1}^{K}\frac{(r_i - 1 + \lambda_i)}{r_i}\phi_i\ln\left(\sum_{j=1}^{K}\phi_j f_{ij}\right) \quad (15)$$

The parameter λ characterizing the long-distance correlations was determined by MC results of critical temperatures and compositions for two binary polymer systems with chain lengths $r_1 = 1$, $r_2 = 4$ and 200 (Yan *et al.*, 1996; Panagiotopoulos and Wong, 1998). The long-range correlations for a branched polymer are apparently different from those of a linear polymer with the identical molecular weight, although they both have $r - 1$ neighboring pairs. Similar to Hawker et al. (Hawker *et al.*, 1991), a parameter $D_b = (N_\perp + N_h - 2)/r$ has been introduced to characterize the degree of branching (Yang *et al.*, 2006b), where $N_\perp$ represents the number of ways in which three bonds meet up at a lattice site (Nemirovsky *et al.*, 1987); N_h is the number of head units of a polymer chain. By this definition, the degree of branching of linear polymers is naturally equal to zero. The increase in the degree of branching D_b enhances the segment contacts and the long-range correlations. Finally, the parameter λ can be calculated by

$$\lambda_i = \frac{z(r_i - 1)(r_i - 2)(1 + D_{bi})}{6r_i^2}(0.1321r_i + 0.5918) \quad (16)$$

This equation can be used for polymers of arbitrary D_b in a lattice with arbitrary z.

2.6 Comparisons with molecular simulation results

The above molecular thermodynamic model for polymer systems has been widely tested by comparing with simulation results (Yang *et al.*, 2006a; Xin *et al.*, 2008a). Figure 8 shows the comparisons between predicted critical temperature and critical volume fraction for binary polymer solutions at different chain lengths of with the

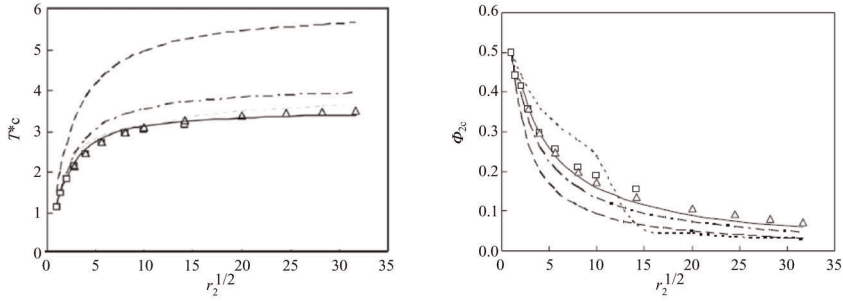

Figure 8 Chain-length dependence of the reduced critical temperature and the critical volume fraction. Square and triangle: MC data; solid line: this work; dot-dashed line: this work with $\lambda = 0$; dash line: Flory–Huggins's theory; dotted line: Freed theory (Yang *et al.*, 2006a).

simulated results of Yan et al. (Yan *et al.*, 1996) and Panagiotopoulos and Wong (Panagiotopoulos and Wong, 1998). Figure 9 shows the comparisons between simulated coexistence curves (Yan *et al.*, 1996; Panagiotopoulos and Wong, 1998) with predictions of our model for binary polymer solutions with chain lengths up to $r_2 = 600$. Figure 10 shows the comparison between simulated spinodals (Rodriguez *et al.*, 1992) with predictions by various theories for systems with $r_2 = 18$ and 60.

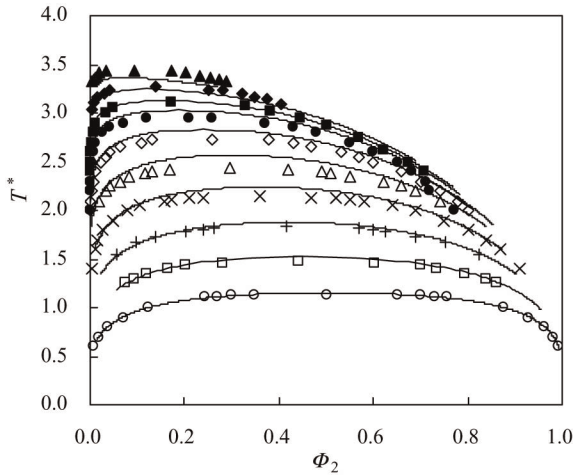

Figure 9 Coexistence curve of binary polymer solutions with different chain lengths. From bottom to top: the chain lengths are 1, 2, 4, 8, 16, 32, 64, 100, 200, and 600, respectively.

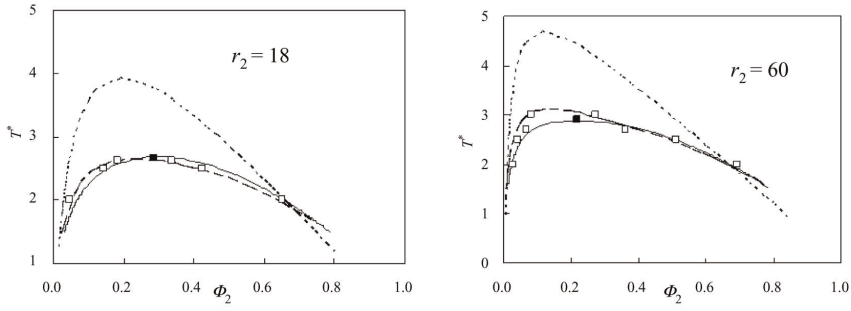

Figure 10 Coexistence curve of binary polymer solutions with chain length $r_2 = 18$ and 60. Open squares: MC data; solid line: this work; dash line: Flory–Huggins theory; dotted line: Freed theory.

Figure 11 shows the coexistence curves of branched polymers L, B2, and D with r_2 = 65 and different architectures. The predictions from this model agree very well with MC data (Arya and Panagiotopoulos, 2005), particularly at high-polymer volume fractions. Figure 12 illustrates the comparisons between calculated binodal curves by the RFT (Chen *et al.*, 2005), this work (Xin *et al.*, 2008b), and corresponding simulation data (Chen *et al.*, 2000; Chen *et al.*, 2005) for random

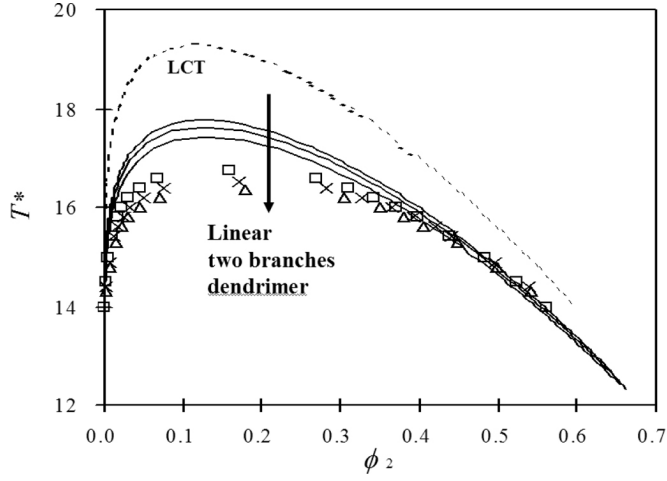

Figure 11 Coexistence curves of branched polymer solutions with $r_2 = 65$ and different architectures (Yang *et al.*, 2006b). MC data: squares (L), crosses (B2), triangles (D); solid line: this work; dotted line: LCT.

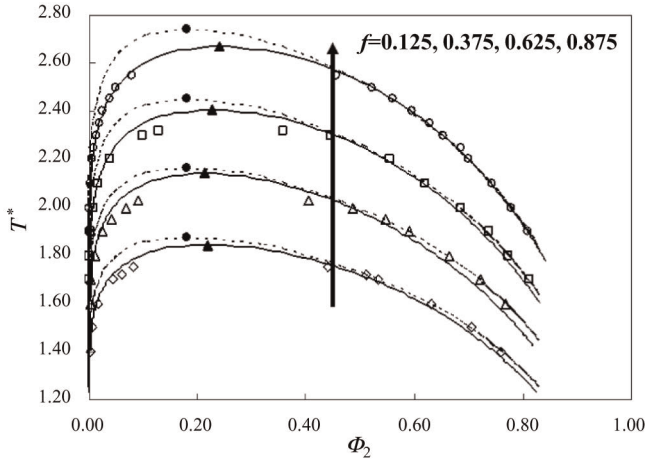

Figure 12 Coexistence curves for lattice random copolymers with different chain compositions ε_{AA}:ε_{AB}:ε_{BB} = 1.0:0.8:0.6, $r_s = 1$, $r_p = 32$(Xin *et al.*, 2008b). Solid line: this work; dotted line: RFT.

copolymer systems where the chain length is held fixed at 32 but the chain composition varies, the employed interaction energy parameters are ε_{AA}:ε_{AB}:ε_{BB} = 1.0:0.8:0.6. Figure 13 shows the predicted LLE of ternary polymer solutions with type 1 and type 2 phase separation. The MC data are taken from (Jiang *et al.*, 1997; Xin *et al.*, 2008a; Liu *et al.*, 2007). The liquid–liquid phase equilibria of ternary chain-like mixtures predicted by this model are in good agreement with MC simulation

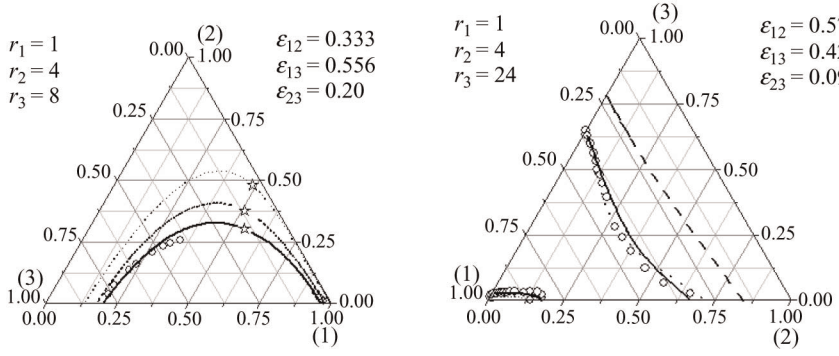

Figure 13 Liquid–liquid equilibria phase diagrams of ternary polymer solutions (Xin *et al.*, 2008a). Open circles: the simulated results; dotted lines: Flory–Huggins; short-dot lines: RFT; solid lines: this work.

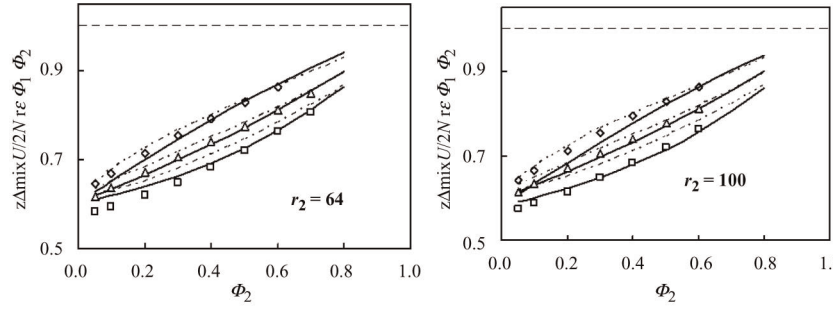

Figure 14 Normalized internal energy of mixing for a binary polymer solutions with $r_2 = 64$(Yang *et al.*, 2006a) and 100. MC data: $kT/\in = 4$ (open square); $kT/\in = 10$ (open triangle); $kT/\in = -10$ (open diamond); solid lines: this work; dotted line: Freed theory; dash line: Flory–Huggins theory.

results. All three types of phase separations of Treybal classification can be described satisfactorily. Figure 14 shows the comparisons between simulated internal energies of mixing $z\Delta_{\text{mix}}U/2N_r\varepsilon\phi_1\phi_2$ (Yang *et al.*, 2006a) with those predicted by various theories for systems with r_2 = 64 and 100. The predicted critical temperatures and critical compositions, spinodals and coexistence curves as well as the internal energies of mixing for systems with various chain lengths are in satisfactory agreement in comparison with simulation results.

2.7 Equation of state for polymer systems based on lattice fluid model

To account for the volume (pressure) effect, a lattice fluid model based on the Flory–Huggins theory was first proposed by Sanchez and Lacombe (Sanchez and Lacombe, 1976; Lacombe and Sanchez, 1976) by assuming complete randomness in the distribution of molecules and holes on the lattice. Hu and coworkers (Hu *et al.*, 1992) adopted a two-step mixing process to introduce holes to the RFT and established another lattice fluid model. Recently, Shin et al. (Shin and Kim, 2006) extended a new quasichemical nonrandom lattice fluid model to describe VLE of mixtures. Panayiotou et al. (Panayiotou *et al.*, 2004) developed a nonrandom hydrogen-bonding model, which was applicable to various systems including nonpolar systems and highly nonideal systems with strong specific interactions, and Tsivintzelis et al. (Tsivintzelis *et al.*, 2006) derived new analytical expressions for the nonrandomness factor, which was used to describe nonrandomness in mixtures, and compared it with others corresponding expressions.

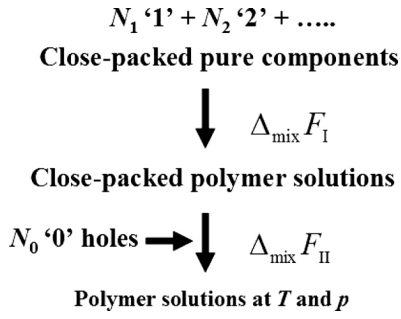

Figure 15 Process of two-step mixing (Xu *et al.*, 2008b).

To extend a close-packed lattice model Equation (15) to a lattice fluid model, we adopt a two-step process as shown in Figure 15 to establish an EOS (Hu *et al.*, 1992). In the first step, pure chain molecules at close-packed lattice are mixed to form a close-packed mixture. In the second step, the close-packed mixture is mixed with N_0 holes to form an expanded realistic system with volume V at temperature T and pressure p. According the two-step process, the Helmholtz energy of mixing can be expressed as

$$\Delta_{\text{mix}}F = \Delta_{\text{mix}}F_I + \Delta_{\text{mix}}F_{\text{II}} \tag{17}$$

Following (Hu *et al.*, 1992), the same model is applied for both steps. In the first step, the Helmholtz energy of mixing $\Delta_{\text{mix}}F_{\text{I}}$ is calculated by Equation (15). In the second step, the close-packed mixture is considered to be a pseudopure substance ''a'', its average segment number r_{a}, and the segment–segment interaction energy parameter ε_{aa} are estimated by $r_a^{-1} = \sum_{i=1}^{K} \phi_i / r_i$ and $\varepsilon_{\text{aa}} = \sum_{i=1}^{K}\sum_{j=1}^{K} \theta_i\theta_j\varepsilon_{ij}$ with $\varepsilon_{ij} = (1-\kappa_{ij})(\varepsilon_{ii}\varepsilon_{jj})^{1/2}$. κ_{ij} is an adjustable parameter and can be correlated from experimental data. Then, N_0 holes are mixed with pseudopure substance ''a'', and the Helmholtz energy of mixing $\Delta_{\text{mix}}F_{\text{II}}$ in this step is

$$\frac{\Delta_{\text{mix}}F_{\text{II}}}{N_r kT} = \frac{1}{\tilde{\rho}}\left\{(1-\tilde{\rho})\ln(1-\tilde{\rho}) + \frac{\tilde{\rho}}{r_a}\ln\tilde{\rho} + \frac{z}{2}\right.$$
$$\left[-(1-\tilde{\rho})\ln[1+(q_a-1)\tilde{\rho}] + \tilde{\rho}\frac{q_a}{r_a}\ln\frac{q_a}{1+(q_a-1)\tilde{\rho}}\right]$$
$$\left. + \frac{z}{2\tilde{T}}(1-\tilde{\rho})\tilde{\rho} - \frac{cz}{4\tilde{T}^2}(1-\tilde{\rho})^2\tilde{\rho}^2 - r_a\frac{-1+\lambda_a}{r_a}\tilde{\rho}\ln\left[\frac{1+(1-\tilde{\rho})D}{1+(1-\tilde{\rho})\tilde{\rho}D}\right]\right\} \tag{18}$$

where $D = \exp(1/\tilde{T}) - 1$, λ_{a} is the parameter characterizing the long-range correlations between monomers in the pseudopure substance ''a''

beyond the close contact pairs and can be obtained by Equation (16). Using classical thermodynamics, we obtain the EOS for mixtures (Xu *et al.*, 2008b; Xu *et al.*, 2009a)

$$\tilde{p} = \tilde{T}\left\{-\ln(1-\tilde{\rho}) + \frac{z}{2}\ln\left[\frac{z}{2}\left(\frac{1}{r_a}-1\right)\tilde{\rho}+1\right]\right\} - \frac{z}{2}\tilde{\rho}^2 - \frac{cz}{4\tilde{T}} \qquad (19)$$

$$(3\tilde{\rho}^4 - 4\tilde{\rho}^3 + \tilde{\rho}^2) + \frac{r_a - 1 + \lambda_a}{r_a}\tilde{T}\tilde{\rho}^2 \frac{[1+(1-\tilde{\rho})D]^2 - 1}{[1+(1-\tilde{\rho})D][1+(1-\tilde{\rho})\tilde{\rho}D]}$$

The reduced temperature $\tilde{T}$, reduced pressure $\tilde{p}$, and reduced density $\tilde{\rho}$ are defined by $\tilde{T} = kT/\varepsilon_{aa}$, $\tilde{p} = p\nu^*/\varepsilon_{aa}$, and $\tilde{\rho} = N_r\nu^*/V$, respectively. Where ν^* is the hard-core volume of a site or a segment.

2.8 Applications for calculations of phase equilibria

Applying the lattice model to practical systems, we have to introduce physically meaningful temperature dependence for the energy parameter due to the oriented interactions between segments. The double-lattice model previously proposed by the authors can provide this relationship (Hu *et al.*, 1991a; Hu *et al.*, 1991b; Hu *et al.*, 1996b). For each type of *i–i*, *j–j*, and *i–j* segment–segment pairs, we imagine a secondary lattice to account for the additional Helmholtz energy originated from various possible arrangements of the oriented and nonoriented interactions. For *i–j* pairs, the total number of sites in the corresponding secondary lattice N_{rij} relates to the number of *i–j* pairs N_{ij} by the conservation relation, $N_{rij}\,z/2 = N_{ij}$. This secondary lattice is an Ising lattice in which the number of sites available for oriented interactions is $N_{rij}\eta_{ij}$, while the remaining $N_{rij}(1-\eta_{ij})$ cannot participate in oriented *i–j* interactions as shown in Figure 16.

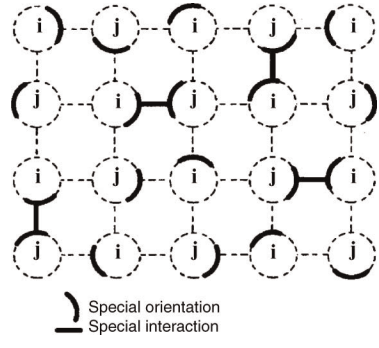

Figure 16 A schematic representation of double lattice model for oriented interactions between molecules *i* and *j* (Hu *et al.*, 1991b).

The additional Helmholtz energy responsible for this secondary lattice can be expressed by using Equation (12) for binary Ising mixture with x_1, x_2 replaced by η_{ij} and $(1 - \eta_{ij})$. Finally, we obtain the temperature-dependent interchange energy that is quadratic to the inverse temperature.

$$\tilde{\varepsilon}_{ij} = \in_{ij}/kT = \left[\delta\varepsilon_{1ij} + \delta\varepsilon_{(2)ij}/kT + \delta\varepsilon_{(3)ij}/(kT)^2\right]/kT \qquad (20)$$

The lattice fluid molecular thermodynamic model described above has been used to calculate phase equilibria including VLE and LLE for systems containing ordinary fluids, polymers, and ionic liquids. Figure 17 shows the calculated spinodal curves and liquid–liquid coexistence curves of PS/cyclohexane systems with temperature-independent energy parameters (Yang *et al.*, 2006a). Figure 18 shows the calculated liquid–liquid coexistence curves of *tert*-butyl acetate/PS and water/poly(ethylene glycol) systems with temperature-dependent

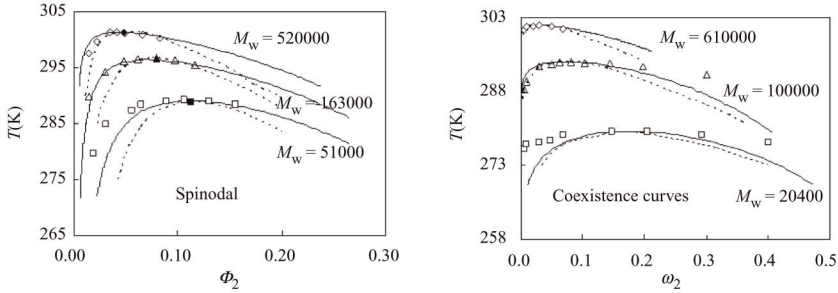

Figure 17 Spinodal curves and coexistence curves of PS/cyclohexane systems (Yang *et al.*, 2006a).

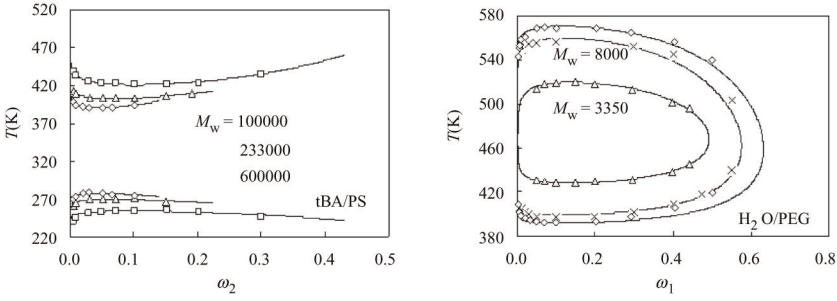

Figure 18 Coexistence curves of *tert*-butyl acetate/PS and water/poly(ethylene glycol) systems (Yang *et al.*, 2006cb).

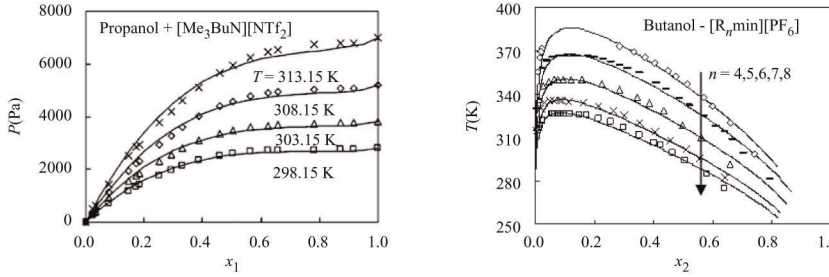

Figure 19 Vapor–liquid equilibria for system of propanol + $[Me_3BuN][NTf_2]$ and liquid–liquid equilibria for system of $[R_n mim][PF_6]$ + Butan-1-ol (Yang *et al.*, 2006d).

energy parameters (Yang *et al.*, 2006cb). Figure 19 shows the VLE for x_1\{propanol\} + $(1 - x_1)$\{$[Me_3BuN][NTf_2]$\} and LLE for x_2\{$[R_n mim][PF_6]$\} + $(1 - x_2)$\{Butan-1-ol\}(Yang *et al.*, 2006d). Combining the Flory's Gaussian chain model for the elastic contribution due to the cross-link between polymers, this model was also used to calculate the swelling behavior of temperature- and/or solvent-sensitive hydrogels in pure or mixed solvents (Huang *et al.*, 2008; Zhi *et al.*, 2010). Figure 20 is the swelling curve (swelling ratio, SR) of PNIPAm gels in ethanol/water mixed solvents at different temperatures.

The EOS based on the lattice fluid model has also be used to describe thermodynamic properties such as *pVT* behaviors, vapor pressures and liquid volumes, VLE and LLE of pure normal fluids, polymers and ionic

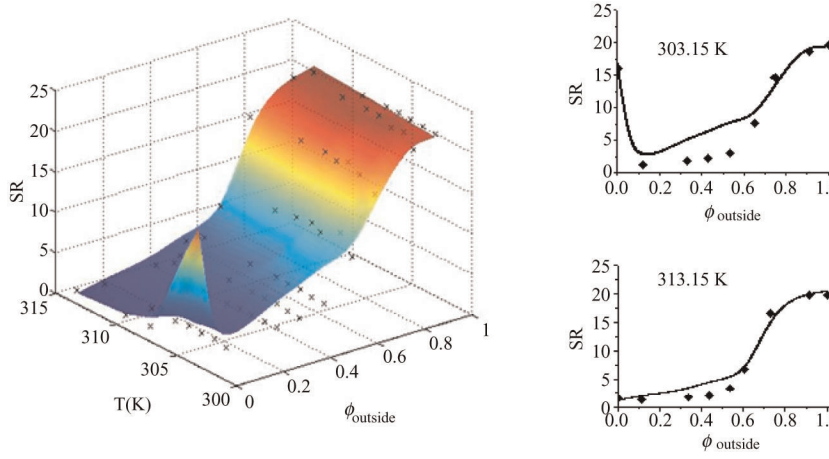

Figure 20 Swelling ratio of PNIPAm gels in ethanol/water mixed solvents (Zhi *et al.*, 2010).

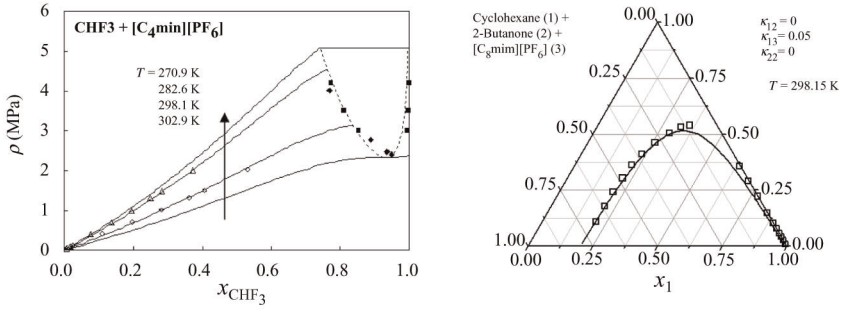

Figure 21 Phase diagrams for mixtures of CHF_3 and $[C_4mim][PF_6]$(Xu *et al.*, 2009b) and the LLE for cyclohexane (1) + 2-butanone (2) + $[C_6mim][PF_6]$ (3) mixture at 298.15 K.

liquids, and their mixtures (Xu *et al.*, 2008b; Xu *et al.*, 2009a; Xu *et al.*, 2009b). Usually, the parameters in an EOS are obtained by correlating experimental *pVT* behavior, vapor pressure, and liquid volume data. For the VLE of binary mixtures, only one adjustable binary interaction parameter was used. The solubility of gas in polymer and ionic liquid can be calculated up to a high pressure. The VLE and LLE of ternary systems containing ionic liquid can be accurately predicted. Figure 21 shows the isothermal *pTx* phase diagrams for mixtures of CHF_3 and $[C_4mim][PF_6]$ and LLE binodal curves for cyclohexane (1) + 2-butanone (2) + $[C_6mim][PF_6]$ (3) mixture at 298.15 K.

3. DENSITY FUNCTIONAL THEORY OF LATTICE BASED POLYMER ADSORPTION

Polymer adsorption at interface plays a key role in many traditional technical fields such as paints, coatings, surface lubricants, ceramics, and adhesives, as well as many emerging areas including self-assembly of functional nanostructures. The layers formed by polymer adsorption have rich structural features because long flexible molecules can adopt a large number of conformations resulting in significant entropic effect. Adsorption of a flexible macromolecule onto an impenetrable surface causes a competition between the reduction in conformational entropy and the energetic compensation of favorable binding. The counterbalance of this competition dominates the molecular conformations and properties of adsorbed polymers. Using different approximations, a series of theoretical models for polymer solutions have been developed based on lattice or off-lattice model. The lattice model provides a simple but effective method for fluids

where the packing effects are not important. Neglecting the packing effects of segments near surface, the adsorption behavior of polymer is exclusively determined by the coupling of conformational entropy and segmental interaction energy.

A number of lattice-based theories have been developed for polymer adsorption (Scheutjens and Fleer, 1979; Simha *et al*., 1953; Ash *et al*., 1970; Helfand, 1975; DeMarzio and Rubins, 1971; Scheutjens and Fleer, 1980; de Gennes, 1980a). Among them, a well-known adsorption theory was proposed by Scheutjens and Fleer (SF) (Scheutjens and Fleer, 1979; Scheutjens and Fleer, 1980). By approximating the partition function of polymer solutions at interface and adopting a matrix method (DeMarzio and Rubins, 1971), they successfully extended the Flory–Huggins theory (Flory, 1941; Huggins, 1941) to predict the adsorption profiles of polymer near solid surface. The mean-field approximation adopted is reasonable at high densities but invalid at low densities (Hu *et al*., 1991a; Hu *et al*., 1996b; Janssen and Nies, 1997). Another approach to polymer adsorption is based on integral equation theory that directly describes the correlations of polymer segments with adsorbing wall (Janssen and Nies, 1997). By neglecting packing effects, Janssen et al. used the discretized polymer–reference interaction site model to calculate the adsorption profiles. With an appropriate closure relation and approximation of the intramolecular two segments distribution function, they obtained improved predictions. To describe the structural and thermodynamic properties of inhomogeneous fluids, DFT is a robust method with the Helmholtz energy density functional of system as its starting point. Over the last two decades, DFT has been successfully applied to inhomogeneous polymeric systems, and most of studies have been focused on the continuum free-space model (Cai *et al*., 2002; Zhang *et al*., 2004; Ye *et al*., 2005; Ye *et al*., 2006; Chen *et al*., 2006a; Ye *et al*., 2007; Chen *et al*., 2007; Chen *et al*., 2008; Woodward *et al*., 1991; Kierlik and Rosinberg, 1992; Yethiraj and Woodward, 1995; Zhou and Zhang, 2001; Yu and Wu, 2002; Patra and Yethiraj, 2000). In the mean time, lattice density functional theory (LDFT) has been proposed for the Ising lattice and for the adsorption of lattice gas. The pioneer work of LDFT is the Ono–Kondo equation (Ono and Kondo, 1960) based on the mean-field approximation. More rigorous treatment is to connect the Helmholtz energy functional with the nonideal interactions through the classical approximation in analogy to the continuum counterpart (Nieswand *et al*., 1993; Reinhard *et al*., 2000; Prestipino and Giaquinta, 2003). Ono–Kondo LDFT has been extended to investigate lattice fluids with various types of molecular structures and intermolecular interactions, including dimers (Aranovich *et al*., 1999;

Aranovich *et al.*, 2000; Chernoff *et al.*, 2002; Chen *et al.*, 2006b). The extension of LDFT to polymer adsorption has been a challenge.

Recently, we presented a LDFT for polymer solutions on a 3D lattice on the basis of an analytical expression of ideal Helmholtz energy density functional for polymer systems (Chen *et al.*, 2009). The excess contributions in the Helmholtz energy density functional are constructed by adopting the close-packed molecular thermodynamic model for polymer solutions described above with either local density approximation (LDA) or WDA. The LDFT developed takes into account the intrinsic energy due to the constraints of connected segments, as well as the site exclusion originated from the excluded-volume effect, the attractive interactions between the nearest neighbors, the long-range correlations from the nonbonded interactions, and their couplings with intrinsic energy. At a special condition, the theory can be used to obtain the equilibrium segment-density distribution for a polymer at interface. By including the correlations between polymer segments due to chain connectivity and attractive interaction, the theory not only predicts the density profiles well but also provides the information of adsorption conformation.

3.1 General formalism

In the lattice representation of a polymer solution, each polymer segment or solvent molecule occupies one lattice site, while the system is regarded as a binary mixture of polymer and solvent. The Helmholtz energy of system can be expressed as

$$F = F^{\mathrm{id}} + \Delta F^{\mathrm{ex}} \tag{21}$$

F^{id} and ΔF^{ex} are the ideal Helmholtz energy functional and excess Helmholtz energy functional, respectively. The ideal Helmholtz energy, as a functional of $\rho_{\mathrm{p}}(\boldsymbol{Q})$ and $\rho_{\mathrm{s}}(\boldsymbol{q})$, can be written as

$$\begin{aligned}\beta F^{\mathrm{id}}[\rho_p(\boldsymbol{Q}), \rho_s(\boldsymbol{q})] &= \beta\langle\hat{H}^{\mathrm{id}}\rangle - \beta T S^{\mathrm{id}} \\ &= \beta\sum_{\boldsymbol{Q}} \rho_p(\boldsymbol{Q}) V_{\mathrm{int}}(\boldsymbol{Q}) + \sum_{\boldsymbol{Q}} \rho_p(\boldsymbol{Q}) \ln\rho_p(\boldsymbol{Q}) \\ &\quad + \sum_{\boldsymbol{q}} \rho_s(\boldsymbol{q}) \ln\rho_s(\boldsymbol{q})\end{aligned} \tag{22}$$

Here subscripts p and s represent polymer and solvent, respectively, $\boldsymbol{Q}$ is the coordinate of all polymers with configurations inherited and $\boldsymbol{q}$ is that of all solvent molecules, $V_{int}(\boldsymbol{Q})$ is the intrinsic energy function. If all the potential terms in addition to the intrinsic energy of r connected segments are taken into account, the real Helmholtz energy functional

of the system can be expressed by

$$\beta F[\rho_p(\boldsymbol{Q}), \rho_s(\boldsymbol{q})] \approx \beta F^{\mathrm{id}}[\rho_p(\boldsymbol{Q}), \rho_s(\boldsymbol{q})] + \beta \Delta F^{\mathrm{ex}}[\rho_m(\boldsymbol{q}), \rho_s(\boldsymbol{q})] \tag{23}$$

The excess part is approximated as a functional of solvent density distribution $\rho_s(\boldsymbol{q})$ and the average segment-density distribution $\rho_m(\boldsymbol{q})$. The latter is related to polymer density $\rho_p(\boldsymbol{Q})$ via a transform as

$$\rho_m(\boldsymbol{q}) \equiv \sum_{Q} \sum_{j=1}^{r} \delta(\boldsymbol{q}_j - \boldsymbol{q}) \rho_p(\boldsymbol{Q}) \tag{24}$$

with $\rho_m(\boldsymbol{q}) + \rho_s(\boldsymbol{q}) = 1$ for incompressible polymer solution, where δ is a Kronecker delta, $\delta(x) \equiv \delta_{0x}$.

3.2 Lattice density functional for a homopolymer solution

We consider a simple cubic lattice with a coordination number $z = 6$. For an incompressible polymer solution, each lattice site is occupied by a solvent molecule or by a segment of polymer chain. The attraction interactions between the nearest-neighbor sites are characterized by a reduced exchange energy $\tilde{\varepsilon} = \beta(\varepsilon_{\mathrm{pp}} + \varepsilon_{\mathrm{ss}} - 2\varepsilon_{\mathrm{ps}})$ between a segment p and a solvent s, where ε_{ij} is the attractive energy of an i–j pair.

3.2.1 Excess Helmholtz energy functional

To construct the excess Helmholtz energy functional ΔF^{ex} for inhomogeneous fluids, the close-packed molecular thermodynamic model for homogeneous bulk fluids described by Equation (15) is used by combining the LDA and nonlocal WDA. The excess Helmholtz energy functional is then separated into the athermal entropy of mixing and the internal energy of mixing,

$$\Delta F^{\mathrm{ex}} = \Delta_{\mathrm{mix}} F_{\mathrm{ather}} + \Delta_{\mathrm{mix}} F_{\mathrm{inter}} \tag{25}$$

Comparing Equation (25) with Equation (23), the approximate density functional of athermal part in Equation (25) can find its counterpart in Equation (23) and is assumed to be

$$\beta \Delta_{\mathrm{mix}} F_{\mathrm{ather}} \xrightarrow{\text{inhomogeneous}} \beta \Delta F^{\mathrm{ex}}_{\mathrm{ather}}[\rho_m(\boldsymbol{q}), \rho_s(\boldsymbol{q})] \tag{26}$$

where

$$\beta \Delta F^{\mathrm{ex}}_{\mathrm{ather}} = \sum_{\boldsymbol{q}} \phi_{\mathrm{ch}}(\rho_m(\boldsymbol{q}), \rho_s(\boldsymbol{q})) \tag{27}$$

This athermal excess Helmholtz energy functional can be estimated via the Staverman–Guggenheim athermal entropy of mixing (Guggenheim, 1952). ϕ_{ch} is a function of ρ_i (i = m, s), representing the segment–segment (intrachain or interchain) and segment–solvent volume repulsions in athermal solution,

$$\phi_{ch}(\rho_m, \rho_s) = \frac{z}{2}\left[\frac{\alpha_r}{r}\rho_m \ln\frac{\alpha_r}{r} - \left(\frac{\alpha_r}{r}\rho_m + \rho_s\right)\ln\left(\frac{\alpha_r}{r}\rho_m + \rho_s\right)\right] \quad (28)$$

where $\alpha_r = [(z-2)r+2]/z$. Because the intersegment volume repulsions are reflected by the ''site exclusion'' within a single lattice site, the LDA can be used to calculate ρ_m. The approximate density functional of the internal energy of mixing in Equation (25) can also find its counterpart in Equation (23). However, the WDA should be adopted. The functional is assumed to be

$$\beta\Delta_{mix}F_{inter} \xrightarrow{\text{inhomogeneous}} \beta\Delta F^{ex}_{inter} = \sum_{q} \rho_m(\boldsymbol{q}) f_{attr}(\overline{\rho}_m(\boldsymbol{q}), \overline{\rho}_s(\boldsymbol{q})) \quad (29)$$

where $\overline{\rho}_i(\boldsymbol{q})$ (i = m, s) is the coarse-grained (weighted) density defined as

$$\overline{\rho}_m(q) \equiv \sum_{q'} w(|q' - q|)\rho_m(q'),\ \overline{\rho}_s(q) = 1 - \overline{\rho}_m(q) \quad (30)$$

$f_{attr}(\rho_m, \rho_s) = f_{am}(\rho_m, \rho_s) + f_{ac}(\rho_m, \rho_s)$, where f_{am} and f_{ac} stand for the contributions from the attractive interactions and the coupling effects between energetic correlation and chain connectivity, respectively. The expressions of the two functions can be obtained through the Helmholtz energy for uniform fluids

$$f_{am}(\rho_m, \rho_s) = \frac{z}{2}\left[\tilde{\varepsilon}\rho_s - \frac{1}{2}\tilde{\varepsilon}^2\rho_m\rho_s^2 - \frac{1}{6}\tilde{\varepsilon}^3\rho_m\rho_s^2(1 - 2\rho_m\rho_s)\right] \quad (31)$$

$$f_{ac}(\rho_m, \rho_s) = -\frac{r - 1 + \lambda_a}{r}\ln\frac{[\exp(\tilde{\varepsilon}) - 1]\rho_s + 1}{[\exp(\tilde{\varepsilon}) - 1]\rho_m\rho_s + 1} \quad (32)$$

where λ_a is a factor accounting for the long-range correlations of polymers and is calculated by Equation (16).

To construct the functional for inhomogeneous fluids and account for the correlations, the coarse-grained densities rather than the local densities should be used. For convenience, we use the Heaviside step function to estimate the weighted densities. In this work, the attraction

exists between nearest neighbors only; therefore, the weighting summation constrained by the Heaviside step function Θ merely runs over the sites adjacent to site q and itself. The weighting function is therefore given by $w(x) \equiv \Theta(x-1)/(z+1)$.

3.2.2 Grand potential and equilibrium density distribution

For the lattice model, the grand potential Ω can be written as

$$\Omega = F + \sum_{Q} \left[V_p^{\text{ext}}(Q) - \mu_p\right]\rho_p(Q) \tag{33}$$

where μ_{p} is the chemical potential and $V_p^{\text{ext}}(Q) = \sum_{j=1}^{r} \nu^{\text{ext}}(q_j)$ is the external potential exerted on all segments. The variational principle gives that the extremum of grand potential corresponds to the equilibrium state of the system, which results in

$$\frac{\delta\Omega}{\delta\rho_p(Q)} = 0 \tag{34}$$

where the functional derivative is equivalent to a partial derivative with respect to $\rho_{\text{p}}(Q)$ in the discrete condition. Substituting Equation (33) into Equation (34) and using Equation (23), the LDFT equation for equilibrium distribution $\rho_{\text{p}}(Q)$ can be obtained as

$$\rho_p(Q) = \exp\left[\beta\mu_p - \beta V_{\text{int}}(Q) - \beta\Psi(Q)\right] \tag{35}$$

where

$$\begin{aligned}\beta\Psi(Q) &= \sum_{j=1}^{r} \beta\varphi(q_j) \\ &= \sum_{j=1}^{r}\left[\frac{1}{r} - 1 - \ln\rho_s(q_j) + \frac{\delta\beta\Delta F^{\text{ex}}}{\delta\rho_m(q_j)} + \nu^{\text{ext}}(q_j)\right]\end{aligned} \tag{36}$$

$$\begin{aligned}\frac{\delta\beta\Delta F^{\text{ex}}}{\delta\rho_m(q)} &= \frac{\delta\beta\Delta F^{\text{ex}}_{\text{ather}}}{\delta\rho_m(q)} + \frac{\delta\beta\Delta F^{\text{ex}}_{\text{inter}}}{\delta\rho_m(q)} \\ &= \frac{\partial\phi_{\text{ch}}}{\partial\rho_m(q)} - \frac{\partial\phi_{\text{ch}}}{\partial\rho_s(q)} + f_{\text{attr}}(\overline{\rho}_m(q), \overline{\rho}_s(q)) \\ &+ \sum_{q'} \rho_m(q') w(|q'-q|)\left[\frac{\partial f_{\text{attr}}}{\partial\overline{\rho}_m(q')} - \frac{\partial f_{\text{attr}}}{\partial\overline{\rho}_s(q')}\right]\end{aligned} \tag{37}$$

Substituting Equation (35) into Equation (24), we finally have the LDFT equation to determine the segment-density distribution as

$$\rho_m(\boldsymbol{q}) = \sum_{\boldsymbol{Q}} \sum_{j=1}^{r} \delta(\boldsymbol{q}_j - \boldsymbol{q}) \exp[\beta\mu_p - \beta V_{\text{int}}(\boldsymbol{Q}) - \beta\Psi(\boldsymbol{Q})] \tag{38}$$

In order to solve Equation (38), we have to know the expression of the intrinsic energy function $V_{\text{int}}(\boldsymbol{Q})$. This function has no contribution to the Helmholtz energy in bulk, thereby it must satisfy the normalizing condition

$$\sum_{\boldsymbol{Q}} \exp[-\beta V_{\text{int}}(\boldsymbol{Q})] = 1 \tag{39}$$

For freely jointed flexible chain, the intrinsic energy can be defined by the r-mer Mayer function of an ideal chain,

$$\exp[-\beta V_{\text{int}}(\boldsymbol{Q})] = \prod_{j=1}^{r-1} \frac{\delta(|\boldsymbol{q}_{j+1} - \boldsymbol{q}_j| - 1)}{z} \tag{40}$$

From Equation (40), Equation (38) can be expressed by

$$\rho_m(\boldsymbol{q}) = \sum_{j=1}^{r} \exp[\beta\mu_p - \beta\varphi(\boldsymbol{q})] G_L^{(j)}(\boldsymbol{q}) G_R^{(j)}(\boldsymbol{q}) \tag{41}$$

Here, the left and right propagator functions, $G_L^{(j)}(\boldsymbol{q})$ and $G_R^{(j)}(\boldsymbol{q})$, are calculated by the following recursive relations

$$G_L^{(j)}(\boldsymbol{q}) = \sum_{\boldsymbol{q}'} \frac{\delta(|\boldsymbol{q}' - \boldsymbol{q}| - 1)}{z} \exp[-\beta\varphi(\boldsymbol{q}')] G_L^{(j-1)}(\boldsymbol{q}') \tag{42}$$

$$G_R^{(j)}(\boldsymbol{q}) = \sum_{\boldsymbol{q}'} \frac{\delta(|\boldsymbol{q}' - \boldsymbol{q}| - 1)}{z} \exp[-\beta\varphi_i(\boldsymbol{q}')] G_R^{(j+1)}(\boldsymbol{q}') \tag{43}$$

where $j = 1, 2, \cdots, r-1$, and $G_L^{(1)}(\boldsymbol{q}) = G_R^{(r)}(\boldsymbol{q}) = 1$.

3.3 Polymer adsorption at solid–liquid interface

The LDFT equation near a planar solid surface can be rewritten as

$$\rho_m(k) = \frac{\rho_b}{r} \sum_{j=1}^{r} \exp[\beta r\varphi_b - \beta\varphi(k)] G_L^{(j)}(k) G_R^{(j)}(k) \tag{44}$$

where $\varphi_b = \varphi(\infty)$, that is, the value of φ with the bulk density ρ_b, and the propagator function $G^{(j)}_{L(R)}(k)$ can be calculated by Equation (42) or Equation (43).

The segment-density distributions of train, loop, and tail form can be calculated by LDFT,

$$\text{train} \quad \rho_{train} = \rho_m(1) \tag{45}$$

$$\text{loop} \quad \rho_{loop}(k) = \frac{\rho_b}{r}\exp\left[\beta r\varphi_b - \beta\varphi(k)\right]\sum_{j=1}^{r} G^{(j)}_A(k)G^{(r+1-j)}_A(k) \tag{46}$$

$$\text{tail} \quad \rho_{tail}(k) = \frac{2\rho_b}{r}\exp\left[\beta r\varphi_b - \beta\varphi(k)\right]\sum_{j=1}^{r} G^{(j)}_A(k)G^{(r+1-j)}_F(k) \tag{47}$$

where $G^{(j)}_A(k)$ can be calculated by Equation (42) or Equation (43) with the condition $G^{(1)}_A(k) = \delta(k-1)$ and $G^{(j)}_A(1) = G^{(j)}(1)$. $G^{(j)}_F(k) = G^{(j)}(k) - G^{(j)}_A(k)$.

The LDFT performs quite well at high densities and the deviations from simulation become distinct when the chain connectivity is important at low densities, long-chain polymers, or low temperatures. Figure 22 plots the normalized surface coverage $\rho^*(1)$ versus the bulk density of an athermal (upper line) and thermal (lower line) 30-mer polymer from the LDFT. The symbols denote the results from MC simulation of (Janssen and Nies, 1997). It is seen that the ρ_b dependence

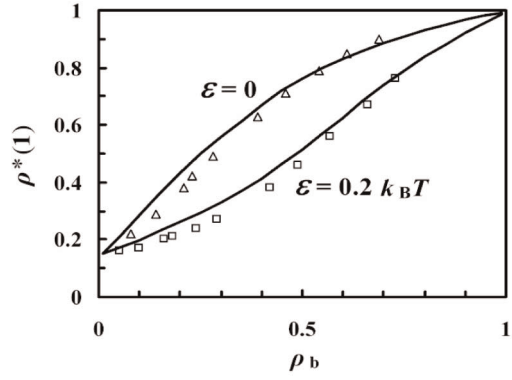

Figure 22 Normalized surface coverage versus the bulk density of 30-mer polymer from LDFT (Chen *et al.*, 2009).

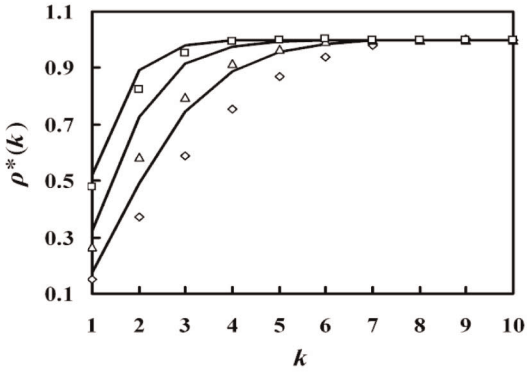

Figure 23 Total segment-density distributions of thermal 40 mers. ρ_b = 0.108, 0.311, 0.51 from bottom to top (Chen *et al.*, 2009).

of $\rho^*(1)$ is reasonably accurate at all bulk densities, especially at $\rho_b > 0.5$. At low density ($\rho_b < 0.5$), the overestimation of LDFT is somewhat distinct. Figure 23 shows comparisons between theoretical prediction and MC data for the total segment-density distributions of a thermal case with $r = 40$.

4. MESO-STRUCTURES OF POLYMER MELTS CONFINED IN CURVED SURFACES

Considerable attention has been paid to the self-aggregation of diblock copolymers primarily due to their ability to form periodical spatial meso-structures such as the body-centered cubic, the hexagonal, and the lamellar structures Both theoretical and experimental approaches have demonstrated that the morphologies of block copolymer melts are essentially controlled by molecular architecture, polymerization index, composition, external fields, and many others. These micro-phase structures can be used as templates to prepare duplicated nanomaterials. For instance, Hashimoto's group (Mita *et al.*, 2008) has produced a polymer template with the macroscopic orientation of hexagonally packed cylinders by imposing a moving temperature-gradient field. Rider (Rider *et al.*, 2008) have migrated polystyrene-*b*-poly(ferrocenylethylmethylsilane) diblock copolymers into silica colloidal crystals and inverse silica colloidal crystals.

The formation mechanism of micro-phase structures for block copolymers essentially roots in a delicate balance between entropic and enthalpic contributions to the Helmholtz energy. Several theories have

been developed. Leibler (Leibler, 1980) calculated the mean-field thermodynamic potential by using the random phase approximation. The Strong Segregation Limit (SSL) theory, originally proposed by Helfand and Wasserman (Helfand and Wasserman, 1976), was further developed by Ohta and Kawasaki (OK) using this approach (Ohta *et al.*, 1986; Ohta and Kawasaki, 1990). The key point in OK theory is that the Helmholtz energy of copolymer melt with micro-phase separation can be divided into two parts: one is contributed by the short-range interaction and another by the long-range interaction, that is, the enthalpic and entropic contribution, respectively. Moreover, the Helmholtz energy density of the enthalpic contribution was assumed to be proportional to the Flory–Huggins interaction parameter between the immiscible blocks, while that of the entropic contribution is scaled to the polymerization index inversely. Later, Fredrickson and Helfand (Fredrickson and Helfand, 1987) extended SSL theory by taking account of fluctuation effects. Following OK theory, SSL theory was improved further to deal with simple graft and star copolymers (Anderson and Thomas, 1988), and calculate the phase diagrams of ABC triblock copolymers (Zheng and Wang, 1995). By utilizing the analytical calculation, instead of the density expansion method in OK theory, Semenov (Semenov, 1989; Semenov *et al.*, 1996) studied both micellization and phase separation in the SSL case. Likhtman (Likhtman and Semenov, 1994; Likhtman *et al.*, 1999) extended Semenov's theory for the stability of ordered bicontinuous double diamond structure and the surface deformations of polymeric brushes in solution.

The external potentials or geometry confinements greatly influence the morphologies of block copolymer melts. The lamellar phase of AB diblock copolymer melts confined between two flat plates has been studied by Turner (Turner, 1992). He found that for surfaces with weak selectivity, either parallel or vertical lamellar structures can be formed depending on the extent of frustration between film thickness and bulk lamellar period. This model was further improved by Walton et al. (Walton *et al.*, 1994) to calculate the Helmholtz energy of both symmetrical and asymmetrical thin films. They found that a critical layer number exists, and above which only the parallel morphology exists symmetrically; whereas, below this number, either vertical or parallel lamellar symmetrical structures can be predicted depending on the deformation of chain. The experiments on the P(S-*b*-MMA) thin films confirmed their predictions (Lambooy *et al.*, 1994; Kellogg *et al.*, 1996).

More recently, many studies have been reported on the micro-phase separation of block copolymers with multidimensional confinements including cylindrical and spherical shapes. Shin and Xiang's group (Shin *et al.*, 2004; Xiang *et al.*, 2004; Xiang *et al.*, 2005a) observed the

phase behavior of polystyrene-*block*-polybutadiene by transmission electron microscopy (TEM). Via a capillary action, the diblock copolymer was drawn into nanoporous alumina membranes to produce free-standing nanorods with a variety of pore diameters. The similar way was also adopted by Sun et al. (Sun *et al*., 2005) to prepare polystryrene-*block*-poly(methyl methacrylate) nanorods, in which the diameter-dependence of the morphologies was systematically investigated by varying the pore diameters of templates from 400 nm down to 25 nm. More experimental results on the cylindrical confinement of block copolymers were reported in (Xiang *et al*., 2005b; Ma *et al*., 2006). More researches focused on simulation and the theoretical analysis (He *et al*., 2001; Sevink *et al*., 2001; Feng and Ruckenstein, 2006a; Feng and Ruckenstein, 2006b; Chen *et al*., 2006c; Chen and Liang, 2007; Li *et al*., 2006; Li and Wickham, 2006; Sevink and Zvelindovsky, 2008; Xiao *et al*., 2007; Zhu and Jiang, 2007; Yu *et al*., 2006; Yu *et al*., 2007a; Yu *et al*., 2007b; Yu *et al*., 2007c; Wang *et al*., 2008a; Wang *et al*., 2008b; Wang, 2007; Han *et al*., 2008). A wide variety of morphologies for block copolymers confined in a cylinder such as the so-called ''multibarrel-layer,'' ''dart-board,'' or ''concentric cylinder barrel'' was predicted by simulation (He *et al*., 2001) and DDFT (Sevink *et al*., 2001). As consistent with experimental results, Yu et al. (Yu *et al*., 2006; Yu *et al*., 2007a; Yu *et al*., 2007b; Yu *et al*., 2007c) systematically investigated the morphologies of AB diblock copolymers under multidimensional confinements via the lattice MC simulation. Inspired from Wang's work (Wang, 2007), a simple model for the layer thickness of concentric lamellae in both 2D and 3D confined systems was proposed for symmetrical diblock copolymers (Yu *et al*., 2007b; Yu *et al*., 2007c), where the accurate layer thicknesses was calculated based on the lattice model and compared with Wang's theoretical prediction. In a ring-like curved confinement, Han et al. (Han *et al*., 2008) studied the effect of disperse index on the morphology of diblock copolymers and found that such effect acts directly on the formation of concentric cylinder structures.

In general, if a ring-like curved surface selects one of the blocks strongly, parallel lamellar structures (or concentric-ring barrel structures) will occur. If the surface is neutral or weakly preferential, however, more complex structures such as the sector column and the multilayer sector column will form. Theoretically, the molecular thermodynamic model described in Section 2 can be used to calculate the Helmholtz energy of this system, and the equilibrium complex structures can be obtained by minimizing the Helmholtz energy. However, the interfacial Helmholtz energy should be accounted in this case due to the existence of interfaces among different meso-domains. In this work, the Semenov's approach is adopted to deduce the Helmholtz energy of

AB diblock copolymers confined in ring-like curved surfaces. Both strong and weak preferences to different block from the curved surfaces will be discussed. Especially, the Helmholtz energy confined in a nanopore can be obtained once the interior radius approaches to zero. For a strong preferred surface in a nanopore, to predict structural lamellar transition, MC simulations are carried out to investigate symmetrical and asymmetrical concentric cylinder barrel structures, and the Helmholtz energy profiles are plotted as a function of dimensionless radius. However, for a weak preferred surface in a nanopore, the discussions are mainly done for symmetrical parallel lamellar and sector column phases. Comparing this graph with simulation results, we found a conflict of compatibilities caused by neglecting other possible morphologies. Consequently, the topological morphology of complex multilayered sector column (CMSC) structure is extracted theoretically from MC simulation.

4.1 Monte Carlo simulation for diblock copolymers confined in curved surfaces

In order to develop a theoretical method for describing the mesostructures of diblock copolymer confined in curved surfaces, MC simulation was first used to find the possible phase separation structures of diblock copolymer melt.

4.1.1 Diblock copolymers confined in cylindrical pore

4.1.1.1 Strong preference to block copolymer. A cylindrical pore with a size of $R_{ex} \times L_z$ was used in the simulation, where R_{ex} is the exterior radius of pore and $L_z = 50$ is the length of pore. The periodic boundary condition was applied in the axial direction $\varepsilon_{AB} = 0.5k_BT$ is the interaction energy between A and B segments, while $\varepsilon_{AS} = -\varepsilon_{BS} = -1.0k_BT$ is the interaction energy between the block and the exterior pore surface. Those interaction energy parameters suggest that the interaction between blocks and B is repulsive, the surface has strong attractive interaction with block A and strong repulsive interaction with block B. The volume concentration of the A_5B_5 diblock copolymer is 90%.

In order to determine the thickness of each layer for the concentric cylinder barrel structure, the radial order parameter, $\psi(r) = \langle \phi_A(r) - \phi_B(r) \rangle / \langle \phi_A(r) + \phi_B(r) \rangle$, was introduced, where $\phi_A(r)$ is the density of A blocks at r, and $< >$ denotes the ensemble average. $\psi(r) > 0$ means the rich A layer at r and $\psi(r) < 0$ otherwise. Figure 24a and b plot $\psi(r)$ with $R_{ex}/L_0 = 1.39$ and 1.80 corresponding to $N_{layer} = 1.5$ and 2, respectively. It is shown that the symmetrical cylinder barrel in Figure 24b possesses

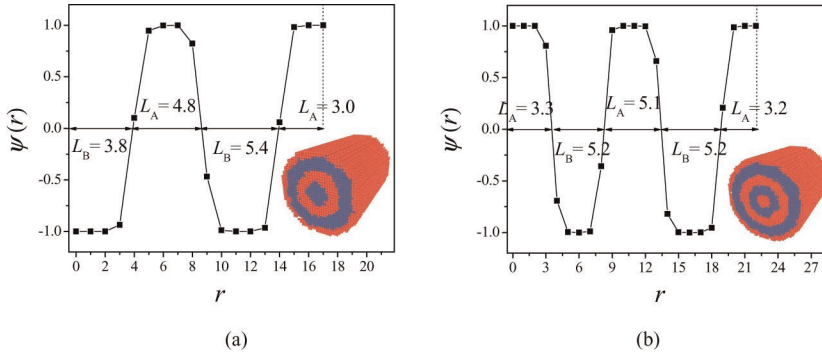

Figure 24 $\psi(r)$ profiles at varying R_{ex}/L_0: (a) $R_{ex}/L_0 = 1.39$, $N_{layer} = 3/2$ and (b) $R_{ex}/L_0 = 1.80$, $N_{layer} = 2$.

the same fringe thickness at both outmost and innermost layer, and at each middle layer, whether it belongs to A domain or not, nearly twice the thickness of the fringe layers. As for the asymmetrical structure in Figure 24a, the alternative ABAB concentric cylinder barrel can be considered as a combination of symmetrical ABA and AB with half a period. All the remarks can be confirmed through the data in Figure 24.

The morphology transition of multilayered structures can be quantitatively determined by $\psi(r)$. Figure 25a reveals the relationship between N_{layer} and R_{ex}/L_0. It can be seen that symmetrical structure occurs at about $R_{ex}/L_0 = n$, while asymmetrical structure at about $R_{ex}/L_0 = n + (1/2)$, where n is an integer. Before or after these transition points, the excess relaxation or compression in each layer space causes the deviation from the characteristic period L_0. The circles with sparse bias in Figure 25a indicate the transition points at $R_{ex}/L_0 = 1.14$ and 1.72, corresponding to $N_{layer} = 1$ and 1.5, respectively. Due to the perturbed frustration between R_{ex} and L_0 before these transition points, a significant deformation, instead of the perfect circle, occurs in the center phase of the pores, as shown in Figure 25b and c. In Xiang's experiments (Xiang *et al.*, 2004), the deformation in the center phase for either PS or PBD was also observed by TEM, which agrees well with our simulation.

4.1.1.2 Weak preference to block copolymer. Figure 26 shows the MC simulated morphologies of A_5B_5 diblock copolymers confined in cylindrical nanopores with the different exterior radii R_{ex} and $\varepsilon_{AS} = \varepsilon_{BS} = 0$. It is shown that the lamellar structure forms parallel to the pore axis. However, there is a little difference between small and large R_{ex}. The lamellar structure is not bended at small R_{ex} as shown in Figure 26a, while it is bended like the wave-shape at large R_{ex} as

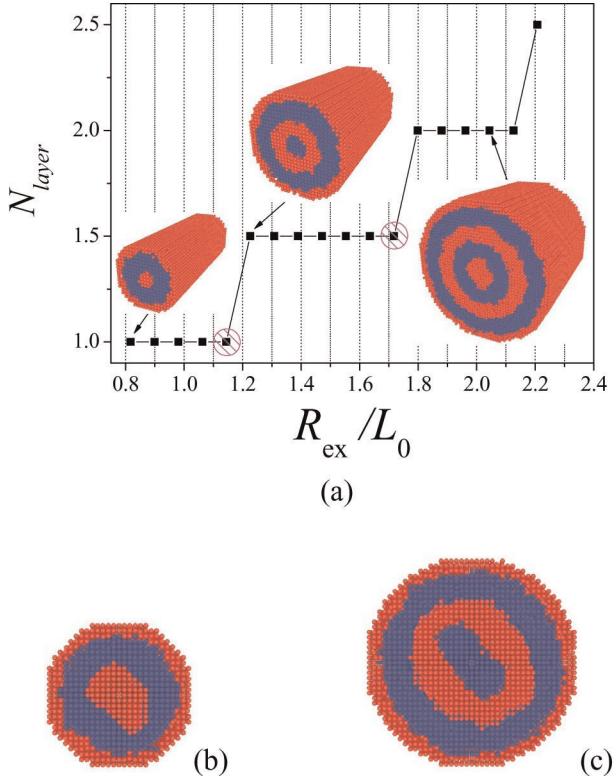

Figure 25 (a) For concentric cylinder barrel, N_{layer} versus R_{ex}/L_0 is plotted. The circles with sparse bias mark the transition points at $R_{ex}/L_0 = 1.14$ and 1.72, respectively. Parts b and c are the snapshots corresponding to $N_{layer} = 1$ and 1.5, respectively.

shown in Figure 26b–e. There are four small collective phase regions approximated by the concentric square column structure phase. The statistical average values of gyration radius of diblock copolymer chains show that the plane (x, y) component is more than 4.0 and the perpendicular component is nearly 1.0. This indicates that AB diblock copolymer chains are relatively compressed in the z direction, whereas they are relatively stretched and ellipse-like along the plane (x, y). Additionally, the up-and-down periodical change in gyration radius of diblock copolymer chains with R_{ex} is observed, which implies that even though an ellipse-like packing along the plane (x, y), AB diblock copolymer chains would also shrink and spread alternately with the increase of R_{ex}. It is consistent with the prediction by SSL theory shown later.

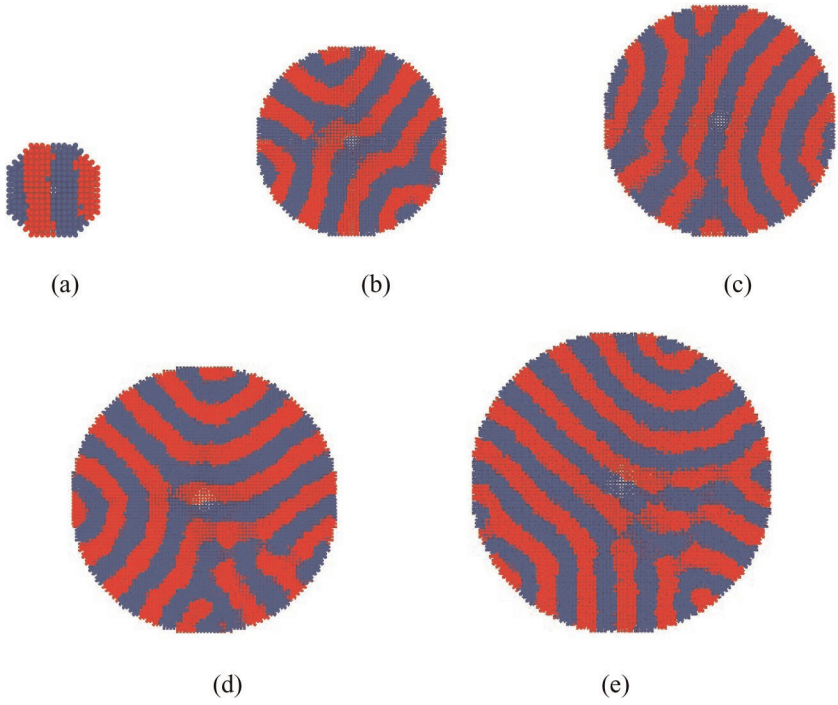

Figure 26 Micro-phase morphologies of A_5B_5 diblock copolymer melts in cylindrical nanopore as the neuter exterior surface when varying the exterior radius R_{ex}. $\varepsilon_{AB} = 0.5k_BT$; $\varepsilon_{AS} = \varepsilon_{BS} = 0$. Red: A block; blue: B block. (a) $R_{ex} = 9$; (b) $R_{ex} = 30$; (c) $R_{ex} = 35$; (d) $R_{ex} = 40$; (e) $R_{ex} = 45$.

4.1.2 Diblock copolymers confined between two concentric curved surfaces

When the confined surfaces suffer from a weak interaction with block copolymer, either parallel or vertical lamellar structures for AB diblock copolymer systems under flat and curved confinements could exhibit, as shown in Figure 27. From theoretical predictions (Turner, 1992; Walton *et al.*, 1994) and simulations (Wang *et al.*, 2000; Yin *et al.*, 2004), the frustration between d and L_0 could result in the alternative appearance of parallel lamellar and vertical lamellar structures under flat confinements. A question is naturally arisen: can both concentric cylinder barrel and sector column structures appear under the curved confinement?

The morphologies of AB diblock copolymers confined between two concentric curved surfaces with exterior radii R_{ex} and interior radii R_{in} have been investigated via MC simulations in our previous work

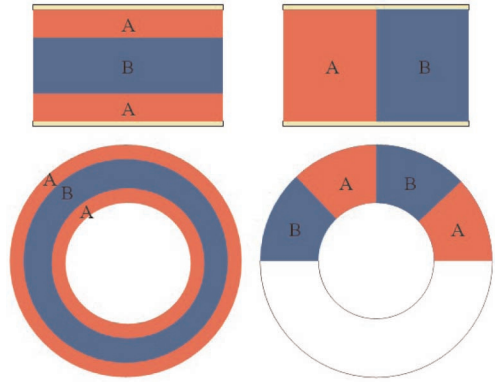

Figure 27 Schematic illustrations of lamellar morphologies for AB diblock copolymers under flat and curved confinements. The concentric cylinder barrel structure under curved confinement corresponds to the parallel lamellar structure under flat confinement (left). The sector column structure corresponds to the vertical lamellar structure (right).

(Xiao *et al.*, 2007). The results indicate that the regular parallel lamella structure (the concentric cylinder barrel structure) appears if d and L_0 are compatible in both flat and curved confinements, while a vertical or distorted vertical lamellae structure (sector column structure) is observed otherwise. Upon increasing the curvature of the exterior surface $K = 1/R_{ex}$, the compatibility span of d and L_0 becomes smaller; consequently, the formation of the parallel lamella structure (or the concentric cylinder barrel structure) is more difficult. Our MC results in this work are shown in Figure 28 and more details can be referred to (Xiao *et al.*, 2007).

The effect of curvature on the morphology transition of AB diblock copolymers by MC simulation is illustrated in Figure 29 (corresponding to Figure 8 in (Xiao *et al.*, 2007)). When $d/L_0 = 0.735$, d and L_0 are compatible from Figure 28a, a parallel lamellar structure occurs at $N_{layer} = 1$ and $K = 0$ as observed from Figure 29a. When K increases, the incompatibility between d and L_0 becomes more acute, and more vertical lamellar domains along with the thickness emerge as shown in Figure 29b–d. Figure 29c shows the typical coexisting vertical and parallel lamellar structure of AB diblock copolymers. A series of simulations prove that the distorted vertical lamellar structure, rather than the perfect sector column and concentric cylinder barrel structures, forms more readily at the higher K because of its lower Helmholtz energy, which is also classified as the incompatible region in Figure 28b–c.

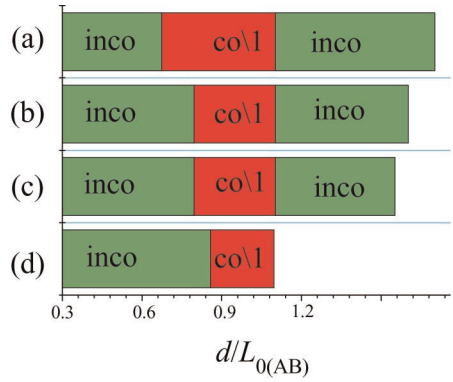

Figure 28 Effect of $d/L_{0(AB)}$ (MC simulation result origins from Figure 9 in (Xiao *et al.*, 2007)) on morphology transitions of AB copolymers at different curvature K of (a) 0; (b) 0.03125; (c) 0.04167; and (d) 0.0625. "inco" means "incompatible region," while "co\n" is a compatible region between d and $L_{0(AB)}$ with $N_{layer} = n$.

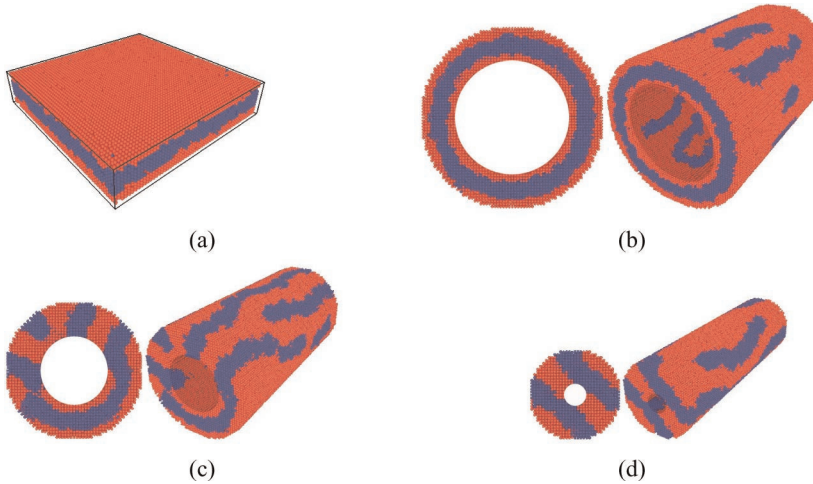

Figure 29 Morphologies of AB diblock copolymers confined in symmetry surfaces with various K at $d/L_{0(AB)} = 0.735$. Red: A blocks; blue: B blocks. K: (a) 0; (b) 0.03125; (c) 0.04167; and (d) 0.0625.

4.2 SSL theory for diblock copolymers confined in ring-like curved surfaces

According to the MC simulation results mentioned above, if the diblock copolymer melts are confined in cylindrical pore or between two concentric curved surfaces with strong preference to one of the blocks, the

concentric-ring barrel structures can be observed. However, if the interactions between polymer block and surfaces are weak, the sector column structures or more complex structures may appear. Those irregular complex structures can be considered as the combination of simple regular phase separation structures. In order to theoretically describe those structures, the Helmholtz energies of simple regular phase separation structures are first derived by using SSL theory in the following sections.

The SSL theory regards chemically distinct blocks to be completely immiscible. The Helmholtz energy of the molten diblock copolymer system consists of two contributions: one is the interfacial energy F_{int} and the other the elastic energy of blocks F_{st}. In Semenov's SSL theory (Likhtman and Semenov, 1994; Semenov, 1985), the excess Helmholtz energy per copolymer chain is simplified and expressed as:

$$F = N\sigma_{\text{AB}}\frac{S_0}{V_0} + \frac{3\pi^2}{8f_\alpha^2 Na^2 V_0}\int_{[\alpha]} z(\boldsymbol{r})^2 \mathrm{d}\boldsymbol{r} \tag{48}$$

where N is the polymerization degree of block copolymers, σ_{AB} is the interfacial tension of A and B domains expressed by the Flory–Huggins parameter χ as $\sigma_{\text{AB}} = a(\chi/6)^{1/2}$, V_0 is the volume of a Wigner–Seitz cell, S_0 is the interfacial area per cell, f_α is the volume fraction of α block and a is the statistical bond length. The model system contains n monodispersed diblock copolymer chains confined in two concentric curved surfaces with a size of $R_{\text{ex}} \times R_{\text{in}} \times L_z$, where L_z is the length at z direction, R_{ex} and R_{in} are the exterior and interior radii. The thickness is $d = R_{\text{ex}} - R_{\text{in}}$, and the curvature is $K = 1/R_{\text{ex}}$. The symmetric exterior and interior surfaces prefer to attract A segments but are repulsive to B segments. σ_{AS} (or σ_{BS}) defines the interfacial tension between A domain (or B domain) and the two surfaces. In this work, the average concentration of segments $\rho(=nN/V)$ is assumed to be unity.

4.2.1 Helmholtz energy of symmetrical parallel lamellar confined in ring-like curved surfaces

Figure 30 shows the symmetrical concentric-ring barrel structure $(\text{A–B–A})_m$ confined between two ring-like curved surfaces (cylinders). It is assumed that the fringe thickness is the same for both the exterior and interior layers, while that of the middle layers is nearly twice in size regardless of A domain or B domain. This assumption has been proved to be valid via MC simulation mentioned above.

The length of the circular lamellar period is L. A variable d is set to denote the thickness of the barrel structure, $d = mL$, m is the number of periods. From Figure 30, the interfacial Helmholtz energy of a barrel

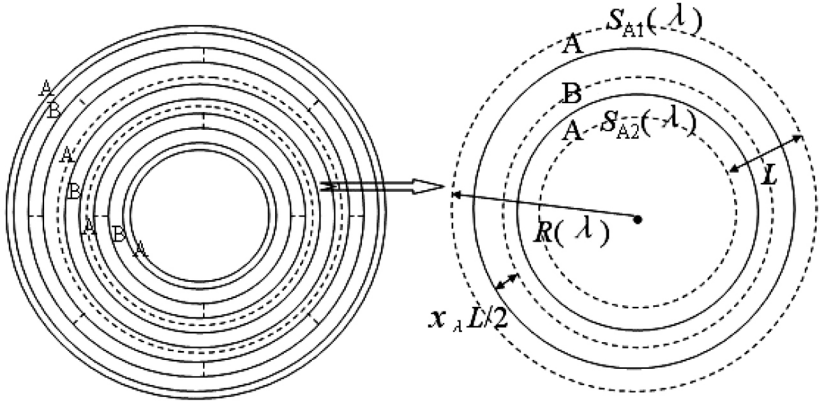

Figure 30 Symmetrical concentric-ring barrel structure (left) confined in the ring-like surface and a unit cell with one lamellar period L (right).

structure characterized by d or m per copolymer chain can be expressed as

$$\begin{aligned} F_{\text{int}}^{\text{Sym}} &= \frac{1}{n_c}\left[\sum_{\lambda=1}^{m} 2\pi\left[\left(R(\lambda)-\frac{f}{2}L\right)+\left(R(\lambda)-L+\frac{f}{2}L\right)\right]\times L_z\right] \\ &\quad \times \sigma_{\text{AB}} + \frac{2\pi}{n_c}(2R_{\text{ex}}-d)L_z\sigma_{\text{AS}} \\ &= 2m\sigma_{\text{AB}}\frac{\pi L_z(2R_{\text{ex}}-d)}{n_c} + 2\sigma_{\text{AS}}\frac{\pi L_z(2R_{\text{ex}}-d)}{n_c} \end{aligned} \tag{49}$$

where n_c is the number of copolymer chains, subscripts S and ex denote the wall surface and the exterior surface, L_z is the length of cylinder, and f is the asymmetrical parameter of diblock copolymers. Obviously, f cancels out in Equation (49), which indicates that the asymmetry of AB diblock copolymers has no effect on the interfacial Helmholtz energy. Equation (49) can be further simplified with $\rho = n_c N/V$.

$$F_{\text{int}}^{\text{Sym}} = \frac{2N}{\rho d}(m\sigma_{\text{AB}} + \sigma_{\text{AS}}) \tag{50}$$

As for the elastic Helmholtz energy of a single chain, applying Equation (48) to A block gives

$$F_{\text{st}}^{A} = \frac{3\pi^2 L_z}{8f^2 N a^2 V}\sum_{\lambda=1}^{m}\int_{[S_A(\lambda)]} z(\boldsymbol{r})^2 \mathrm{d}\boldsymbol{r} \tag{51}$$

The conformational integral is calculated by

$$\int_{[S_A(\lambda)]} z(\boldsymbol{r})^2 \, \mathrm{d}\boldsymbol{r} = \int_0^{fL/2} 2\pi \left[R(\lambda) - \frac{fL}{2} + r \right] r^2 \mathrm{d}r + \int_0^{fL/2} 2\pi \left[R(\lambda) - L + \frac{fL}{2} - r \right] r^2 \mathrm{d}r = \frac{\pi f^3 L^3}{12} [2R(\lambda) - L] \tag{52}$$

By combining Equation (52) with Equation (51), the elastic Helmholtz energy of A block can be obtained as

$$F_{\mathrm{st}}^A = \frac{\pi^3 L_z f L^3}{32 N a^2 V} \times m(2R_{\mathrm{ex}} - mL) \tag{53}$$

Similarly, the elastic Helmholtz energy of B block can be obtained from Equation (48). For a unit cell shown in Figure 30, the distortion can be estimated by

$$(f + x_\lambda) \left(2R(\lambda) - \frac{f + x_\lambda}{2} L \right) = 2R(\lambda) - \frac{f}{2} L \tag{54}$$

where x_λ is the distortion coefficient of B block in the λth cell. Hereby, the conformational integral is extended as

$$\int_{[S_B(\lambda)]} z(\boldsymbol{r})^2 \mathrm{d}\boldsymbol{r} = 2\pi \left[\frac{x_\lambda^3 L^3}{24} \left(R(\lambda) - \frac{f}{2} L \right) - \frac{x_\lambda^4 L^4}{64} + \frac{L^3}{3} \left(1 - f - \frac{x_\lambda}{2} \right)^3 \times \left(R(\lambda) - L + \frac{f}{2} L \right) + \frac{L^4}{4} \left(1 - f - \frac{x_\lambda}{2} \right)^4 \right] \tag{55}$$

The elastic Helmholtz energy of B block can be written as

$$F_{\mathrm{st}}^B = \frac{3\pi^2 L_z}{8(1-f)^2 N a^2 V} \sum_{\lambda=1}^{m} \int_{[S_B(\lambda)]} z(\boldsymbol{r})^2 \mathrm{d}\boldsymbol{r} \tag{56}$$

By combining Equation (53) with Equation (56), the elastic Helmholtz energy of AB diblock copolymer chain can be obtained.

Finally, after substituting Equations (50), (53), and (56) into Equation (48), the excess Helmholtz energy F^{Sym} per copolymer

chain can be further simplified and formulated as a function of d and m,

$$F^{\mathrm{Sym}} = \frac{2N}{\rho d}(m\sigma_{\mathrm{AB}} + \sigma_{\mathrm{AS}}) + \frac{f\pi^2}{32Na^2}L^2 + F^B_{\mathrm{st}} \tag{57}$$

4.2.2 Helmholtz energy of asymmetrical parallel lamellar confined in ring-like curved surfaces

Figure 31 shows the structure of an asymmetrical concentric-ring barrel confined in ring-like curved confinements. Different from the symmetrical one, the exterior and interior rings in the asymmetrical system are not the same. In order to calculate the free energy, the asymmetrical ring barrel is considered as $(\mathrm{A–B–A})_M$–A–B, which is composed of a symmetrical multilayered structure and an asymmetrical one with half a period. In this way, the Helmholtz energy F^{Asy} can be separated into two parts: one is F^{Sym} of the symmetrical multilayered structure and the other is the Helmholtz energy of the asymmetrical one with half a period. By setting $d = ML + L/2$, M is the number of symmetrical periods. The symmetrical part F^{Sym} has been presented in above section. Because the innermost cell of the cylinder is one A–B unit with half a period $L/2$, the distortion coefficients of A and B blocks, f' and x', must accord with the following equations

$$f\left(2R_{\mathrm{ex}} - \frac{4M+1}{2M+1}d\right) = f'\left(2R_{\mathrm{ex}} - \frac{4M+f'}{2M+1}d\right) \tag{58}$$

and

$$f' + x' = 1 \tag{59}$$

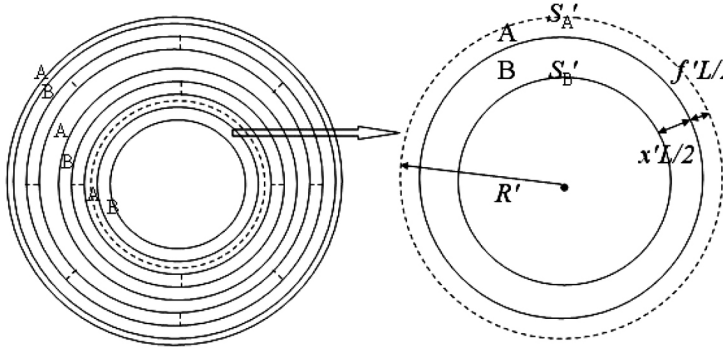

Figure 31 Asymmetrical structure of concentric-ring barrel (left) and the inner cell with half an period (right).

The interfacial contribution to the Helmholtz energy per copolymer chain can be expressed as

$$F_{\text{int}}^{\text{Asy}} = \frac{1}{n_c}\left[\sum_{\lambda-1}^{M} 2\pi\left[\left(R(\lambda) - \frac{fL}{2}\right) + \left(R(\lambda) - L + \frac{fL}{2}\right)\right] \times L_z\right]\sigma_{\text{AB}} + \frac{1}{n_c}\left[2\pi \times \left[R(M) - L - \frac{f^{'}L}{2}\right] \times L_z\right]$$

$$\sigma_{\text{AB}} + \frac{2\pi L_z}{n_c}[(\sigma_{\text{AS}} + \sigma_{\text{BS}})R_{\text{ex}} - \sigma_{\text{BS}}d]$$

$$= \frac{2M\sigma_{\text{AB}}N}{\rho d(2R_{\text{ex}} - d)}\left(2R_{\text{ex}} - \frac{2M}{2M+1}d\right) + \frac{2\sigma_{\text{AB}}N}{\rho d(2R_{\text{ex}} - d)}\left(R_{\text{ex}} - \frac{2M + f^{'}}{2M+1}d\right) + \frac{2N[(\sigma_{\text{AS}} + \sigma_{\text{BS}})R_{\text{ex}} - \sigma_{\text{BS}}d]}{\rho d(2R_{\text{ex}} - d)} \tag{60}$$

The elastic Helmholtz energy $F_{\text{st}}^{\text{Asy}}$ of AB diblock copolymer chain can be expressed by a sum of $F_{\text{st}}^{\text{Sym}}$, $F_{\text{st}}^{(\text{A})\text{Asy}}$, and $F_{\text{st}}^{(\text{B})\text{Asy}}$ as

$$F_{\text{st}}^{\text{Asy}} = F_{\text{st}}^{\text{Sym}} + F_{\text{st}}^{(\text{A})\text{Asy}} + F_{\text{st}}^{(\text{B})\text{Asy}} \tag{61}$$

where $F_{\text{st}}^{\text{Sym}}$ is the contribution from the symmetric part, $F_{\text{st}}^{(\alpha)\text{Asy}}$ denotes the elastic Helmholtz energy of α block in the innermost cell. According to Equations (53) and (56), $F_{\text{st}}^{\text{Sym}}$ can be expressed as

$$F_{\text{st}}^{\text{Sym}} = \frac{\pi^2 f L^3}{32Na^2d(2R_{\text{ex}} - d)} \times M(2R_{\text{ex}} - ML) + F_{\text{st}}^{\text{B(Sym)}} \tag{62}$$

When $M=0$, $F_{\text{st}}^{\text{B(Sym)}} = 0$; otherwise, $F_{\text{st}}^{\text{B(Sym)}} = \dfrac{3\pi}{8(1-f)^2Na^2d(2R_{\text{ex}} - d)} \sum_{\lambda=1}^{M} \int z(\boldsymbol{r})^2 \mathrm{d}\boldsymbol{r}$.
$[S_B(\lambda)]$

In the A–B unit with half a period, the elastic Helmholtz energy of each block can be evaluated by

$$F_{\text{st}}^{(\text{A})\text{Asy}} = \frac{3\pi^2}{4f^2Na^2d(2R_{\text{ex}} - d)}\left[\left(R_{\text{ex}} - \frac{2M + f^{'}}{2}L\right) \times \frac{f^{'3}L^3}{24} + \frac{f^{'4}L^4}{64}\right] \tag{63}$$

and

$$F_{\text{st}}^{(\text{B})\text{Asy}} = \frac{3\pi^2}{4(1-f)^2Na^2d(2R_{\text{ex}} - d)}\left[\left(R_{\text{ex}} - d + \frac{x^{'}}{2}L\right) \times \frac{x^{'3}L^3}{24} - \frac{x^{'4}L^4}{64}\right] \tag{64}$$

By combining Equations (62), (63), and (64) with Equation (61), the elastic Helmholtz energy of AB diblock copolymer chain can be obtained. Finally, we have F^{Asy} by adding Equation (50) to Equation (51).

4.2.3 Helmholtz energy of sector column confined in ring-like curved surfaces

As shown in Figure 32, the sector column phase can also be considered as the distortion of the vertical lamellae phase in the flat plates system, which is a counterpart to the above parallel lamellae. With the assumption of the repeated number of basic A–B unit in the cylinder, and the interval angle of basic unit, $\theta = 2\pi/M$, M is the number of sectors, the interfacial contribution per copolymer chain can be expressed as:

$$\begin{aligned} F_{\mathrm{int}}^{\mathrm{Sec}} &= \frac{2MdL_z\sigma_{\mathrm{AB}}}{n} + \frac{1}{n}[2f\pi(2R_{\mathrm{ex}} - d)L_z\sigma_{\mathrm{AS}} + 2(1-f)\pi(2R_{\mathrm{ex}} - d)L_z\sigma_{\mathrm{BS}}] \\ &= \frac{2MN\sigma_{\mathrm{AB}}}{\pi\rho(2R_{\mathrm{ex}} - d)} + \frac{2N}{\rho d}[\sigma_{\mathrm{BS}} + f(\sigma_{\mathrm{AS}} - \sigma_{\mathrm{BS}})] \end{aligned} \tag{65}$$

Similar to the abovementioned method, the entropic contribution of single chain of sector column phase can be written as

$$F_{\mathrm{st}}^{A} = \frac{3\pi^2 ML_z}{4f^2Na^2V} \int_{[S'_A]} z(\boldsymbol{r})^2 \mathrm{d}\boldsymbol{r} \tag{66}$$

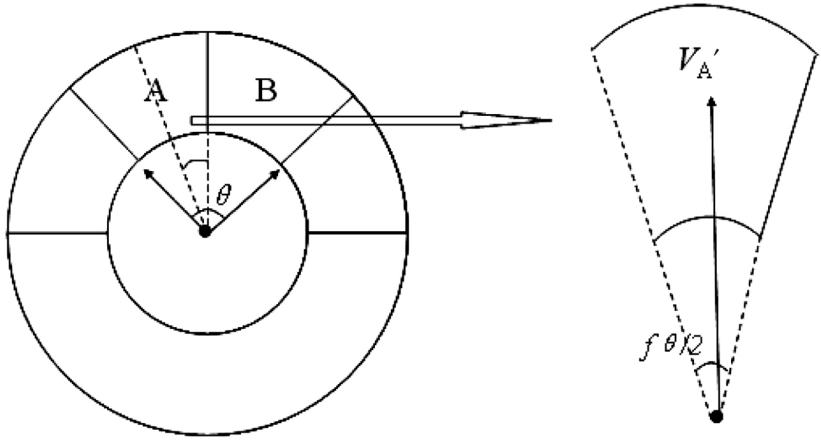

Figure 32 Sector column structure (left) and the unit cell with half period of A domain (right).

with $\int_{[S'_A]} z(\boldsymbol{r})^2 \mathrm{d}\boldsymbol{r} = \int_0^{f\theta/2} \int_{R_{in}}^{R_{ex}} R^3 \sin^2\varphi \mathrm{d}R\mathrm{d}\varphi = (1/16)(R_{ex}^4 - R_{in}^4)(f\theta - \sin f\theta)$ and the Taylor polynomial expansion, $\sin x = x - x^3/3! + O(x^3)$, Equation (66) can be simplified as

$$F_{st}^A = \frac{\pi M(R_{ex}^2 + R_{in}^2) f\theta^3}{128Na^2} = \frac{\pi^4 f(2R_{ex}^2 - 2R_{ex}d + d^2)}{16Na^2M^2} \tag{67}$$

The same way can be used to derive the entropic contribution of B block.

The Helmholtz energy F^{Sec} of sector column phase in SSL is the sum of F_{int}^{Sec} and F_{st}^{α}. Furthermore, considering $M = \pi(2R_{ex} - d)/L_0$ with $L_0 = 2(\sigma_{AB}/3\rho)^{1/3}(aN)^{2/3}$ is the bulk lamellae period, we get the simplified expression Equation (65) of sector column structure:

$$F^{Sec} = \left(\frac{3N\sigma_{AB}^2}{\rho^2 a^2}\right)^{1/3} + \frac{2N}{\rho d}[\sigma_{BS} + f(\sigma_{AS} - \sigma_{BS})] + \frac{\pi^2}{12}\left(\frac{3N\sigma_{AB}^2}{\rho^2 a^2}\right)^{1/3} \times \frac{2 - 2Kd + K^2d^2}{4 - 4Kd + K^2d^2} \tag{68}$$

In this work, we assume $\sigma_{BS} = -\sigma_{AS}$. Equation (68) indicates that F^{Sec} is a function of both thickness d and curvature K.

4.3 Application to phase separation of diblock copolymer confined in two curved surfaces

The Helmholtz energy expressions derived above for symmetrical and asymmetrical parallel lamellae (concentric-ring barrel) and sector column structures can be extended to flat surface systems. The comparisons between the curved and flat systems will not be introduced in detail here; however, some conclusions can be shared as follows: the concentric-ring barrel structure is the same as the parallel lamellar essentially; the difference exists in the bending Helmholtz energy that is zero in the flat confinement; when the curvature K increases, the change of bending Helmholtz energy must not be neglected. Consequently, it is well founded that the flat confinement is merely a special case of the ring curved confinement with $K \to 0$.

4.3.1 Strong preference of the curved surfaces to block copolymer

The morphologies of polystyrene-*b*-polybutadiene (PS-*b*-PBD) diblock copolymers confined in a nanopore were observed by Shin and Xiang (Shin *et al.*, 2004), in which a lot of attentions were paid to the layer number of the concentric cylinder barrel structure as a function of the nanopore radius. In this work, the symmetrical and asymmetrical

parallel lamellar mentioned in Section 4.2 are adopted to study this problem.

In a nanopore confinement, the Helmholtz energy of both symmetrical and asymmetrical concentric cylinder barrel phases can be obtained by taking $d \rightarrow R_{ex}$ in Equation (57) and Equation (60)–(64). In order to compare with the above MC simulation quantitatively, the same parameters were selected. In addition, the statistical bond length in SSL (a = 1.29) was calculated by an ensemble-average bond length over all the collected configurations in MC simulation.

Figure 33 plots the Helmholtz energy profiles of both symmetrical and asymmetrical cylinder barrels along with R_{ex}/L_0. Both are similar to the undulated wave. At a small R_{ex}/L_0, the fluctuations of Helmholtz energy are intensified because of the bending. With increasing R_{ex}/L_0, the two curves oscillate periodically, indicating the periodic adjustment of the multilayer number. Meanwhile, the Helmholtz energy at a higher R_{ex}/L_0 converges to the intrinsic state of the bulk phase. The corresponding layer numbers N_{layer} of the two curves are also plotted synchronously, in which the transitions of both structures are indicated at a

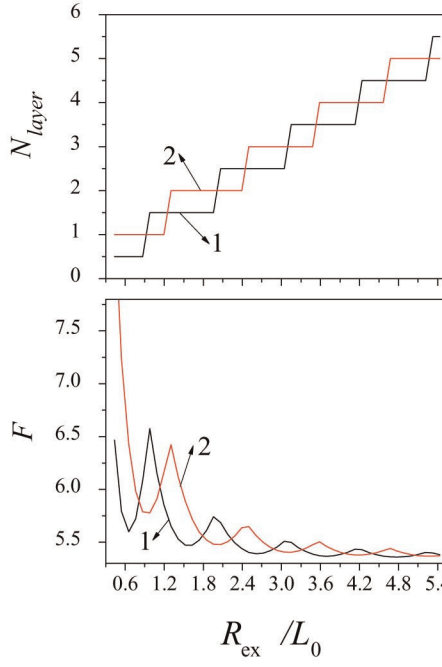

Figure 33 Helmholtz energy profiles and N_{layer} versus R_{ex}/L_0. Line 1: asymmetrical structure; line 2: symmetrical structure.

certain R_{ex}/L_0. Line 1 denotes the asymmetrical structure, while line 2 indicates the symmetrical one. It is obvious that the N_{layer} transition of line 1 occurs at $n + (1/2)$, while that of line 2 merely at n, where n is an integer. There are many cross-points between line 1 and line 2 in Figure 33, which implies the mutual transition between the two morphologies at a certain R_{ex}/L_0. By minimizing the Helmholtz energy before and after the cross-points, a continuous profile of the total energy can be plotted as a function of R_{ex}/L_0, and the transition of N_{layer} along with R_{ex}/L_0 in Figure 34. In the interval [0.4–5.5] of R_{ex}/L_0, the exposed structure with higher frequencies is the asymmetrical cylinder barrel with $N_{layer} = n + (1/2)$, which is very consistent with simulations shown in Figure 25a.

For the direct comparison with our MC simulation, SSL theory and the results of other simulations and experiment quantitatively, a detailed summarization for N_{layer} is listed as a function of R_{ex}/L_0 in Table 1. There are several sources of different simulations and experimental data taken from Wang (Figure 3 in (Wang, 2007)), Sun et al.

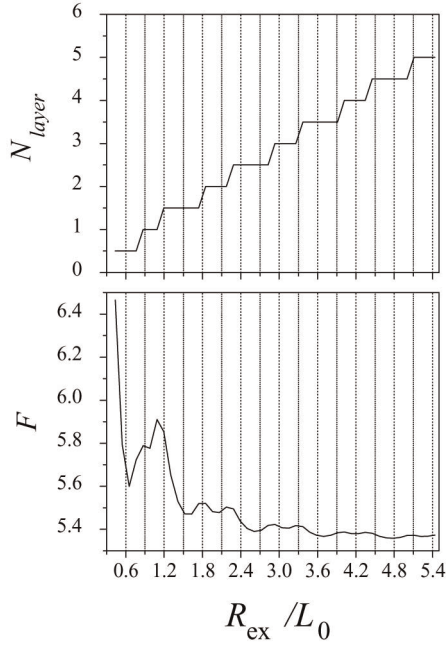

Figure 34 Total Helmholtz energy profile and the corresponding layer transition are plotted as a function of R_{ex}/L_0, which are obtained by minimizing free energy of two kinds of the morphologies in Figure 33.

Table 1 N_{layer} versus R_{ex}/L_0 in MC simulation, SSL theory and experiments

R_{ex}/L_0					N_{layer}	R_{ex}/L_0					N_{layer}
MC	SSL	Wang's sim	Sun et al.'s exp	Xiang et al.'s exp		MC	SSL	Wang's sim	Sun et al.'s exp	Xiang et al.'s exp	
	0.43	0.500	0.32		0.5		2.93				3
	0.54				0.5		3.04				3
	0.65				0.5		3.15				3
	0.76				0.5		3.26				3
0.82	0.87	0.791	0.77	0.95 ($N_{layer} = 0.5$)	1.0		3.37				3.5
0.90	0.98	1.067			1.0		3.48				3.5
0.98	1.09				1.0		3.59				3.5
1.06					1.0		3.70				3.5
1.14					1.0		3.80				3.5
							3.91				3.5
1.23	1.20	1.344		1.30 ($N_{layer} = 1.0$)	1.5						
1.31	1.30				1.5		4.02			4.05	4
1.39	1.41				1.5		4.13				4
1.47	1.52	1.500		1.60	1.5		4.24				4
1.55	1.63				1.5		4.35				4
1.64	1.74				1.5						
1.72					1.5						

(Continued)

TABLE 1 *(continued)*

R_{ex}/L_0					N_{layer}	R_{ex}/L_0					N_{layer}
MC	SSL	Wang's sim	Sun et al.'s exp	Xiang et al.'s exp		MC	SSL	Wang's sim	Sun et al.'s exp	Xiang et al.'s exp	
1.80	1.85				2.0		4.46				4.5
1.88	1.96				2.0		4.56				4.5
1.96	2.06				2.0		4.67				4.5
2.04	2.17				2.0		4.78				4.5
2.13					2.0		4.89				4.5
							5.00				4.5
2.21	2.28		2.31		2.5		5.11		5.13		5
	2.39				2.5		5.22				5
	2.50				2.5		5.33				5
	2.61				2.5		5.43				5
	2.72				2.5						
	2.83				2.5		...				...

(Figure 4 in (Sun *et al.*, 2005)) and Xiang et al. (Figure 1 in (Shin *et al.*, 2004) and Figure 2 in (Xiang *et al.*, 2005a)). It is worth noticing that the diameter D in their simulations and experiments is related to the dimensionless diameter D/L_0, rather than R_{ex}/L_0 employed in our definition. The N_{layer} values in the parentheses represent the experimental data that are different from our calculations, and all other data without the parentheses are identical to this work.

A significant consistency is observed between MC simulation and SSL. Wang (Wang, 2007) also studied the layer transitions in nanopore by MC simulation and strong stretching theory. Sun et al. (Sun *et al.*, 2005) reported the PS-PMMA diblock copolymers confined in a nanopore, Xiang et al. (Shin *et al.*, 2004; Xiang *et al.*, 2005a) investigated the effect of curved confinement on the morphologies of PS-PBD diblock copolymers. From Table 1, it is found that our predictions are more closely consistent with Wang's simulation results and Sun et al.'s experimental data, but a relative deviation occurs from Shin et al.'s and Xiang et al.'s data at the small R_{ex}/L_0. At $R_{ex}/L_0 = 1.30$, for example, $N_{layer} = 1.5$ in our SSL calculation, but $N_{layer} = 1.0$ in Shin et al.'s and Xiang et al.'s experiments for the concentric cylinder barrel structure. One possible reason may lie in the inaccuracy in their experiments (not a well-defined round nanopore at the small R_{ex}/L_0. Finally, theoretical calculation is found to be very consistent with simulation, and both give good predictions in comparing with experimental results.

4.3.2 Weak preference of the curved surfaces to block copolymer

4.3.2.1 Mutual transformation between the competing morphologies. Figures 35 and 36 show the Helmholtz energies of the concentric cylinder barrel and sector column structures of diblock copolymer melts confined in ring-like curved surfaces as a function of the thickness d. Lines 1 and 2 in Figure 35 are the Helmholtz energies of the concentric cylinder barrel structures for $\sigma_{AS} = 0$ and -0.05, respectively. The lower Helmholtz energies are attributed to more negative σ_{AS} that implies more stable micro-phase structures. Line 3 in Figure 35 is the Helmholtz energy of the sector column structures at different K values, which reveals a rapid increase at large d. At a small d, the Helmholtz energy of the sector column phase is mainly dominated by interfacial energy. As d increases, however, the Helmholtz energy is gradually dominated by conformational entropy. As compared lines 1 and 2 with line 3 in Figure 35a and b, there is a drastic competition occurring at a small d caused by minimizing the Helmholtz energies of two structures. This indicates a notable periodical transformation from the concentric cylinder

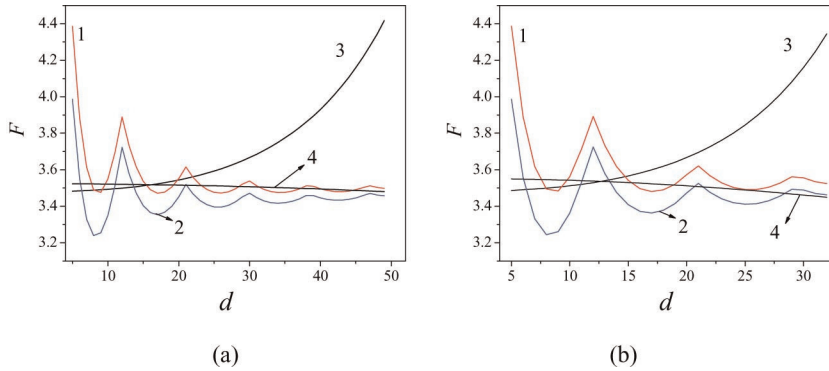

Figure 35 Helmholtz energies predicted by SSL for AB diblock copolymers under curved confinements as a function of the thickness d ($f = 0.5$, $\chi N = 30$, and $N = 20$) at curvatures of $K =$ (a) 0.02 and (b) 0.03. Lines 1 and 2: concentric cylinder barrel structures at $\sigma_{AS} = 0$ and -0.05, respectively; line 3: sector column phase; line 4: complex multilayered sector column phase discussed in Section 4.3.2.3.

barrel to the sector column structures and vice versa. It is hard to form the sector column phase at a high d due to the increasing Helmholtz energy. In order to examine the effect of curvature on the morphology transition for AB diblock copolymer films, Figure 36a summaries lines

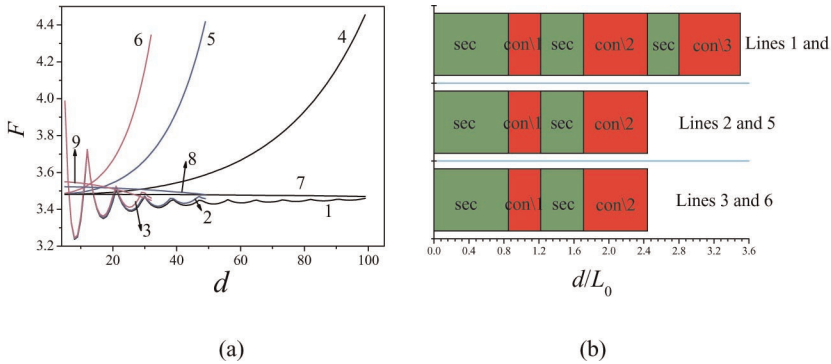

Figure 36 (a) Helmholtz energy predicted by SSL for AB diblock copolymers confined in the different curving surfaces as a function of d at $\sigma_{AS} = -0.05$ ($f = 0.5$, $\chi N = 30$, and $N = 20$). Lines 1–3: concentric cylinder barrel phase at $K = 0.01$, 0.02, and 0.03, respectively; lines 4–6: sector column phase at $K = 0.01$, 0.02, and 0.03, respectively; lines 7–9: complex multilayered sector column phase at $K = 0.01$, 0.02, and 0.03, respectively. (b) A sketch of morphology transition for a set of competing structures between the concentric cylinder barrel phase and the sector column phase in part (a), where "sec" means the sector column phase, and "con\n" means the concentric cylinder barrel structure with $N_{layer} = n$.

(2 and 3) in Figure 35a and b. For the concentric cylinder barrel structures, line 1 in Figure 36a corresponds to $K = 0.01$; lines (2) and (3) in Figure 36a correspond to line 2 in Figure 35a and b. While lines 4–6 in Figure 36a are for the sector column phase with the same $K = 0.01$ and correspond to line 4 in Figure 35a and b. In contrast to lines 4–6 in Figure 36a, it is clear that the upward tendency of sector column structures becomes more sensitive along with increasing K values. With increasing K from 0.01 to 0.03, the thickness d of periodical transformation decreases gradually from 23 to 14. The transformation between concentric cylinder barrel and sector column structures is summarized graphically in Figure 36b.

From Figure 36, when K and d increase, the Helmholtz energy of the sector column phase rises up rapidly. If $K \rightarrow 0$ in Equation (68) (the vertical lamellae structure under the flat confinement), the Helmholtz energy approaches to a constant and is independent of d because the second term of Equation (68) is zero. In Semenov's SSL, the chain configurations are described by the Alexander-de Gennes approximation (de Gennes, 1980b) in which the chain stretch is assumed to be normal to the phase interface. At a large value of Kd, the copolymer chains near the curved surfaces stretch and shrink excessively with a sharp increase of conformational entropy. Obviously, a new phase will come up nearby the exterior surface for a large d resulting in a limited extensibility of the copolymer chains.

4.3.2.2 Complex multilayered sector column structure. In Section 4.32.1, we have estimated the Helmholtz energies of both the concentric cylinder barrel and the sector column structures by SSL theory. It is found that, with increasing the curvature K, SSL theory predicts that the compatible region will increase, this result is in contradiction to MC simulation. This conflict between SSL theory and MC simulation is probably caused by the neglect of some possible morphologies in SSL theory. One of the possible morphologies is the ''CMSC'' structure just as mentioned above. This new phase region might appear near the curved surfaces at a large d.

From the above MC simulation results, a suppositional concentric square column structure is constructed, which is not observed in MC simulation (Yu *et al.*, 2007a) but can be considered as a basic block of the CMSC structure. We plot the same four architectures together forming a close-packed structure in Figure 37. Under curved confinements, the topological CMSC structure can be considered as the cross-sectional concentric circle that truncates the four close-packed square columns with the exterior radii R_{ex}, and the center is at the common corner of the four squares. Among the four square columns, the phase structures of

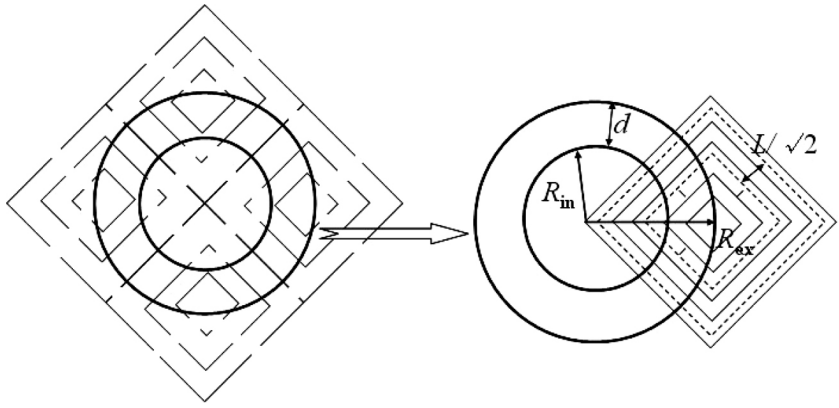

Figure 37 Under curved confinement, when concentric circle scans the close-packed square columns of exterior radius R_{ex}, the topological structure of CMSC would be considered to be a cross-section of concentric circle, whose center is at the common corner of the four squares, exterior and interior radius are R_{ex} and R_{in}, respectively.

neighboring square columns are antisymmetry, while that of diagonal square columns are symmetry. Because of the geometrical confinement of the 2D concentric circles, the Helmholtz energy of the CMSC structure consists of three parts: a term of concentric square columns, a surface tension term, and the bending term from the curved surfaces:

$$F_{\mathrm{CMSC}} = F_{\mathrm{Square}}(R_{\mathrm{ex}}) + \frac{N}{\rho d}(\sigma_{\mathrm{AS}} + \sigma_{\mathrm{BS}}) - \frac{3\pi^2}{64Na^2R_{\mathrm{ex}}^2} \times \left(\frac{\sqrt{2}L}{2}\right)^4 \times \left(\frac{d}{R_{\mathrm{ex}}}\right)^2 \tag{69}$$

When both the exterior and interior surfaces of the confined cylinder are neutral, the second term in Equation (69) equals to zero. If the exterior radius R_{ex} is fixed, F_{CMSC} is only a function of d. $F_{\mathrm{square}}(R_{\mathrm{ex}})$ is the Helmholtz energy of concentric square column phase.

The Helmholtz energy per copolymer chains $F_{\mathrm{Square}}^{\mathrm{Sym}}$ of the symmetrical concentric square column structure can be expressed as

$$F_{\mathrm{Square}}^{\mathrm{Sym}} = \frac{2\sqrt{2}N\sigma_{\mathrm{AB}}}{\rho R_{\mathrm{ex}}} \times \frac{8m^2 + 4m + 1}{8m + 2} + \frac{3\pi^2L^3}{64Na^2R_{\mathrm{ex}}^2}\left[\frac{2m+1}{6}R_{\mathrm{ex}} - \frac{1}{6}\left(m + \frac{1}{2}\right)mL - \frac{L}{32}\right] + F_{\mathrm{st}}^{B} \tag{70}$$

$F_{\text{Square}}^{\text{Sym}}$ is a function of the exterior radius R_{ex} as well as the layer number m. Furthermore, if $m=0$, $F_{\text{st}}^{B}=0$; while $m\neq 0$, $F_{\text{st}}^{B}=\frac{3\pi^2}{4Na^2R_{\text{ex}}^2}\sum_{\lambda=1}^{m}\int_{[S_B(\lambda)]}z(\boldsymbol{r})^2\mathrm{d}\boldsymbol{r}$, where

$$\int_{[S_B(\lambda)]} z(\boldsymbol{r})^2\mathrm{d}\boldsymbol{r}=\frac{1}{4}\left[\frac{x_\lambda^3L^3}{3}\left(R(\lambda)-\frac{L}{4}\right)-\frac{x_\lambda^4L^4}{8}+\frac{(1-x_\lambda)^3L^3}{3}\left(R(\lambda)-\frac{3}{4}L\right)+\frac{(1-x_\lambda)^4L^4}{4}\right] \tag{71}$$

and

$$\left(x_\lambda+\frac{1}{2}\right)\left(2R(\lambda)-\frac{2x_\lambda+1}{4}L\right)=2R(\lambda)-\frac{1}{4}L \tag{72}$$

Similar to the asymmetrical cylinder barrel structure, the asymmetrical square column is considered as a combination of the symmetrical multilayered structure with an asymmetrical one with half a period. The Helmholtz energy $F_{\text{Square}}^{\text{Asy}}$ of the asymmetrical concentric square column structure is separated into two parts: one is the Helmholtz energy $F_{\text{Square}}^{\text{Sym}}$ of symmetrical multilayered structure and another is the Helmholtz energy $F_{\text{Square}}^{\text{Asy}}$ of an asymmetrical one with half a period expressed by

$$\begin{aligned}F_{\text{Square}}^{\text{Asy}}&=F_{\text{int}}^{\text{Asy}}+F_{\text{st}}^{\text{Asy}}\\&=\frac{2\sqrt{2}\sigma_{\text{AB}}N}{\rho R_{\text{ex}}}\times\frac{8M^2+12M+4x'+3}{8M+6}+\frac{3\pi^2L^3}{64Na^2R_{\text{ex}}^2}\\&\times\left[\frac{2M+1}{6}R_{\text{ex}}-\frac{1}{6}\left(M+\frac{1}{2}\right)ML-\frac{L}{32}\right]+F_{\text{st}}^{\text{B(Sym)}}\\&+\frac{3\pi^3}{4Na^2R_{\text{ex}}^2}\left[\left(R_{\text{ex}}-\frac{4M+2f'+1}{4}L\right)\times\frac{f'^3L^3}{12}+\frac{f'^4L^4}{32}\right]+\frac{\pi^2x'^4L^4}{128Na^2R_{\text{ex}}^2}\end{aligned} \tag{73}$$

If $M=0$, $F_{\text{st}}^{\text{B(Sym)}}=0$, while $M\neq 0$, $F_{\text{st}}^{\text{B(Sym)}}=(3\pi^2/4Na^2R_{\text{ex}}^2)\sum_{\lambda=1}^{M}\int_{[S_B(\lambda)]}z(\boldsymbol{r})^2\mathrm{d}\boldsymbol{r}$. In the limit of $d\to R_{\text{ex}}$, f' and x' could be solved by $2f'^2-4f'+1=0$ and $f'+x'=1$. For a given R_{ex}, the minimization of $F_{\text{Square}}^{\text{Asy}}$ is performed with respect to the optimization of m.

4.3.2.3 Helmholtz energy of CMSC structure. In Section 4.32.1, the Helmholtz energies of the two competing structures, that is, the

concentric cylinder barrel and the sector column structures, have been discussed by SSL. Line 4 in Figure 35a and b denotes the Helmholtz energy F_{CMSC} of the CMSC structure, which slightly declines with increasing d. By comparing with other Helmholtz energy profiles, it is easy to find that the CMSC structure tends to form at a high d, while the concentric cylinder barrel and the sector column structures occur mostly at a small d. This is consistent with MC simulation results. Further analyzing the profiles in Figure 35a and b, we see the line 4 is lower than other lines at both higher K and larger d indicating that the CMSC structure is more stable. However, the CMSC structure is not observed at small enough R_{ex} in Figure 36a.

Line 7 in Figure 36 indicates the occurring of the CMSC structure at $K = 0.01$; while lines 8 and 9 are at $K = 0.02$ and 0.03, respectively, corresponding to line 4 in Figure 35a and b. From lines 7–9, one can find that the origo of the Helmholtz energy profiles rises up with increasing curvature K, despite a visible downtrend of the Helmholtz energy F_{CMSC}. Due to the influence of bending, higher Helmholtz energy profiles of square column phase are observed at smaller R_{ex} and larger F_{CMSC}. As a consequence, the CMSC structure is very hard to form at a sufficiently small R_{ex}. Under these conditions, the morphology in Figure 36a is different from others.

4.4 Remarks on the phase separation of confined diblock copolymer

In this work, a framework of the SSL theory for diblock copolymer melts confined in ring-like curved surfaces has been proposed. When the curvature approaches to zero, it reduces to the well-known SSL theory for the parallel lamellar phases. In the case of the equal confined thickness to the exterior radius, it can also be extended to the system with a nanopore confinement. Moreover, the Helmholtz energy of the concentric cylinder barrel, sector column and CMSC phases in 2D confinements based on this SSL theoretical framework can be evaluated in the convenient manner. The calculated results show that the diblock copolymer melts exhibit a layer-type transition with a similar mechanism, regardless of ring-like curved surfaces, planar surfaces, and nanopores.

In this work, we have focused on strong surface preference with only mutual transition between the symmetrical and asymmetrical layer-type structures. SSL theory and MC simulation are further applied to investigate the self-assembled morphology of diblock copolymers confined in the nanopore. MC simulation shows that the N_{layer} of the concentric cylinder barrel changes with respect to the extent of frustration between the exterior radius R_{ex} and the bulk lamellar period L_0. Simultaneously, the predictions of SSL theory also show that both

symmetrical and asymmetrical structures occur periodically by minimizing the Helmholtz energy before and after the cross-points with increasing R_{ex}/L_0. SSL predictions are consistent with MC simulations. Although there are some marginal discrepancies for PS-PBD diblock copolymers, SSL theory for confinement presented in this work shows good agreement with experimental data for PS-PMMA diblock copolymers reported in the literature.

For the surfaces with weak preference, it can be expected for more complex structures with the competition of Helmholtz energy, leading to the morphology transition with the multilayer type. First, two competing micro-phase morphologies of the concentric cylinder barrel and the sector column structures exist for AB diblock copolymers confined between curved surfaces, which resembles the cases of the parallel and vertical lamellar structures confined in planar surfaces. However, theoretical predictions are inconsistent with simulations results due to the neglect of some complicated morphologies in the theoretical framework. Second, we examine a representative complicated morphology of the CMSC structure. From MC simulation, the topological characteristic relationship between the CMSC phase and the concentric square column structure phase is established. Finally, the predicted results are in good agreement with simulation results that the CMSC structure occurs at a higher thickness d, and both the mutually competing concentric cylinder barrel and the sector column structures at a lower d. The reason why the CMSC structure hardly forms at a lower R_{ex} is also unveiled in the theory, which is confirmed by MC simulation.

5. CONCLUSIONS

Many polymer blends or block polymer melts separate microscopically into complex meso-scale structures. It is a challenge to predict the multiscale structure of polymer systems including phase diagram, morphology evolution of micro-phase separation, density and composition profiles, and molecular conformations in the interfacial region between different phases. The formation mechanism of micro-phase structures for polymer blends or block copolymers essentially roots in a delicate balance between entropic and enthalpic contributions to the Helmholtz energy. Therefore, it is the key to establish a molecular thermodynamic model of the Helmholtz energy considered for those complex meso-scale structures. In this paper, we introduced a theoretical method based on a lattice model developed in this laboratory to study the multi-scale structure of polymer systems. First, a molecular thermodynamic model for uniform polymer system is presented. This model can

be successfully used to calculate the *pVT* behavior, VLE and LLE for polymer systems. Combined with DFT, this molecular thermodynamic model can also be used to describe the adsorption of a polymer at a solid–liquid interface and the molecular conformation distribution at interface regions. For the meso-structure of diblock copolymer melts confined in curved surfaces, a SSL theory is presented to study the morphological transition mechanism. The theoretical predicted results are in agreement with MC simulations and experimental observations. It means that the model parameters in the Helmholtz energy model can be obtained by correlating the *pVT* behavior, VLE and LLE of polymer systems. They then can be used, combining with DFT and SSL theory, to predict the adsorption behavior of polymers at solid–liquid interfaces and the meso-structure of polymer melts.

To establish the molecular thermodynamic model for uniform systems based on concepts from statistical mechanics, an effective method by combining statistical mechanics and molecular simulation has been recommended (Hu and Liu, 2006). Here, the role of molecular simulation is not limited to be a standard to test the reliability of models. More directly, a few simulation results are used to determine the analytical form and the corresponding coefficients of the models. It retains the rigor of statistical mechanics, while mathematical difficulties are avoided by using simulation results. The method is characterized by two steps: (1) based on a statistical–mechanical derivation, an analytical expression is obtained first. The expression may contain unknown functions or coefficients because of mathematical difficulty or sometimes because of the introduced simplifications. (2) The form of the unknown functions or unknown coefficients is then determined by simulation results. For the adsorption of polymers at interfaces, simulation was used to test the validity of the weighting function of the WDA in DFT. For the meso-structure of a diblock copolymer melt confined in curved surfaces, we found from MC simulation that some more complex structures exist. From the information provided by simulation, these complex structures were approximated as a combination of simple structures. Then, the Helmholtz energy of these complex structures can be calculated by summing those of the different simple structures.

The macroscopic properties such as mechanical behavior of block copolymers or polymer blends depend directly on the relative concentrations of different constituents and their meso-structures. How to predict the exact macroscopic properties of polymer blends or block copolymers with meso-phase separation structures from pure component properties remains a big challenge. Some theoretical efforts have been explored. For example, Buxton et al. found that the deformations and fractures of polymer blends can be described by the

micromechanical lattice spring model (LSM). Here, the information of the micro-phase separation of polymer blends obtained from the Cahn–Hilliard (CH) model, the lattice Boltzmann model (LBM), or the MD method are taken as the input of the LSM (Buxton and Balazs, 2005; Buxton and Balazs, 2004; Buxton and Balazs, 2003; Buxton *et al*., 2005).

LIST OF SYMBOLS

a	the statistical bond length of polymer
c	empirical constants in the model of Helmholtz energy of mixing in Equation (17)
d	the thickness of block copolymer membrane confined between two concentric curved surfaces
D_b	the branching degree of a branched polymer
F	nonrandom factor defined in Equation (12) or composition of diblock copolymer
F	Helmholtz energy
g	radial distribution function
G	propagator function in Equations (59)–(61)
k	Boltzmann constant
K	number of component in mixture or the curvature of cylindrical pore defined by $K = 1/R_{ex}$
L	the length of cylindrical pore
m	the number of periods in the lamellar
N	the number of molecule in the fluid mixture
N_h	the number of head units of a polymer chain
N_r	total number of sites in lattice model
$N_\perp$	the number of ways in which three bonds meet at a lattice site
P	pressure
q	surface area parameter
$\boldsymbol{q}$	the coordinate of all solvent molecules or polymer segment
$\boldsymbol{Q}$	the coordinate of all polymers with configurations inherited
r	chain length of polymer
R	the radius of cylindrical pore
S	entropy
T	temperature (K)
U	internal energy
v	the external potential exerted on a segment of polymer
v^*	the hard-core volume of a segment of polymer or solvent
V	volume or the external potential exerted on all segments
w	weighting function in DFT
x	mole fraction or the distortion coefficient of block
z	coordination number of a lattice

χ Flory–Huggins parameter
ε interaction energy between segments of polymer or between the segment of polymer and solvent
ϕ volume fraction
Ω the grand potential
η surface fraction of a segment of polymer that can participate in oriented interaction
Ψ function defined by Equation (54)
λ a parameter accounting for the long-range correlations beyond the close contact pair
μ chemical potential
θ surface fraction
ρ density of fluid
σ the interfacial tension
$\in$ the exchange energy between segments of different components

ACKNOWLEDGMENTS

This work is supported by the National Natural Science Foundation of China (Project No. 20736002), Program for Changjiang Scholars and Innovative Research Team in University (No. IRT0721), and the 111 Project (No. B08021). The authors also would like to thank Dr. Jianwen Jiang of Department of Chemical and Biomolecular Engineering of National University of Singapore for his comments and revisions in the preparation of this paper.

REFERENCES

Anderson, D. M. and Thomas, E. L., *Macromolecules* **21**, 3221 (1988).
Aranovich, G. L., Donohue, P. S. and Donohue, M. D., *J. Chem. Phys.* **111**, 2050 (1999).
Aranovich, G. L. and Donohue, M. D., *J. Chem. Phys.* **112**, 2361 (2000).
Arya, G. and Panagiotopoulos, A. Z., *Macromolecules* **38**, 10596 (2005).
Ash, S. G., Everett, D. H. and Findenegg, G. H., *Trans. Faraday Soc.* **66**, 708 (1970).
Bates, F. S., *Science* **251**, 898 (1991).
Bethe, H. A. and Wills, H. H., *Proc. R. Soc.* **A150**, 552 (1935).
Bragg, W. L. and Williams, E. J., *Proc. R. Soc.* **A145**, 699 (1934).
Buxton, G. A. and Balazs, A. C., *Phys. Rev. E* **67**, 031802 (2003).
Buxton, G. A. and Balazs, A. C., *Phys. Rev. B* **69**, 054101 (2004).
Buxton, G. A. and Balazs, A. C., *Macromolecules* **38**, 488 (2005).
Buxton, G. A., Verberg, R., Janow, D. and Balazs, A. C., *Phys. Rev. E* **71**, 056707 (2005).
Cai, J., Liu, H. L. and Hu, Y., *Fluid Phase Equilib* **194-197**, 281 (2002).
Carnahan, N. F. and Starling, K. E., *J. Chem. Phys.* **51**, 635 (1969).
Chaikin, P. M. and Lubensky, T. C., ''Principles of Condensed Matter Physics''. Cambridge, Cambridge University Press (1995).

Chang, B. H. and Bae, Y. C., *Chem. Eng. Sci*. **58**, 2931 (2003) Chang B. H., Bae Y. C., *J. Polym. Sci. B: Polym. Phys*., 42, 1532(2004).
Chang, B. H., Ryu, K. O. and Bae, Y. C., *Polymer* **39**, 1735–1739 (1998).
Chen, P. and Liang, H., *Macromolecules* **40**, 7329 (2007).
Chen, T., Liu, H. L. and Hu, Y., *Macromolecules* **33**, 1904 (2000).
Chen, T., Peng, C. J., Liu, H. L. and Hu, Y., *Fluid Phase Equilib* **233**, 73 (2005).
Chen, H. Y., Ye, Z. C., Peng, C. J., Liu, H. L. and Hu, Y., *J. Chem. Phys* **125**, 204708 (2006).
Chen, Y., Aranovich, G. L. and Donohue, M. D., *J. Chem. Phys*. **124**, 134502 (2006) Chen Y., Aranovich G. L., Donohue M. D., *J. Chem. Phys*., 127, 134903 (2007).
Chen, P., He, X. and Liang, H., *J. Chem. Phys*. **124**, 104906 (2006).
Chen, H. Y., Ye, Z. C., Cai, J., Liu, H. L., Hu, Y. and Jiang, J. W., *J. Phys. Chem. B* **111**, 5927 (2007).
Chen, H. Y., Cai, J., Ye, Z. C., Peng, C. J., Liu, H. L., Hu, Y. and Jiang, J. W., *J. Phys. Chem. B* **112**, 9568 (2008).
Chen, X. Q., Sun, L., Liu, H. L., Hu, Y. and Jiang, J. W., *J. Chem. Phys*. **131**, 044710 (2009).
Chen, H. Y., Chen, X. Q., Ye, Z. C., Liu, H. L. and Hu, Y., *Langmuir* **26**, 6663 (2010).
Chernoff, M. P., Aranovich, G. L. and Donohue, M. D., *J. Chem. Phys* **116**, 9395 (2002).
Cummings, P. T. and Stell, G., *Mol. Phys*. **51**, 253 (1984).
de Gennes, P. G., *Macromolecules* **13**, 1069 (1980).
de Gennes, P. G., *Macromolecules* **13**, 1069 (1980).
DeMarzio, E. A. and Rubins, R. J., *J. Chem. Phys*. **55**, 4318 (1971).
Dudowicz, J. and Freed, K. F., *Macromolecules* **23**, 1519 (1990) Dudowicz J., Freed K. F. *Macromolecules*, **24**, 5076, 5096, 5112(1991).
Dudowicz, J. and Freed, K. F., *Theor. Chim. Acta* **82**, 357 (1992).
Dudowicz, J., Freed, K. F. and Madden, W. G., *Macromolecules* **23**, 4803 (1990).
Feng, J. and Ruckenstein, E., *Macromolecules* **39**, 4899 (2006).
Feng, J. and Ruckenstein, E., *J. Chem. Phys*. **125**, 164911 (2006).
Feng, J., Liu, H. L. and Hu, Y., *Mol. Simul*. **31**, 731 (2005).
Fisher, M. E., *Rep. Prog. Phys*. **30**, 615 (1967).
Flory, P. J., *J. Chem. Phys*. **9**, 660 (1941) Flory P. J., *J. Chem. Phys*., 10, 51(1942).
Fraaije, J. G. E. M., *J. Chem. Phys*. **99**, 9202 (1993).
Fredrickson, G. H. and Helfand, E., *J. Chem. Phys* **87**, 697 (1987).
Freed, K. F., *J. Phys. A: Math. Gen*. **18**, 871 (1985).
Graham, R. S. and Olmsted, P. D., *Faraday Discuss*. **144**, 71 (2010).
Groot, R. D. and Warren, P. B., *J. Chem. Phys*. **107**, 4423 (1997).
Guggenheim, E. A., ''''Mixtures''''. Oxford University Press, Oxford (1952).
Han, Y., Cui, J. and Jiang, W., *Macromolecules* **41**, 6239 (2008).
Hawker, C. J., Lee, R. and Frecbet, J. M. J., *J. Am. Chem. Soc* **113**, 4583 (1991).
He, X., Song, M., Liang, H. and Pan, C., *J. Chem. Phys*. **114**, 10510 (2001).
Helfand, E., *J. Chem. Phys* **63**, 2192 (1975) Helfand E., *Macromolecules*, 9, 307(1976).
Helfand, E. and Wasserman, Z. R., *Macromolecules* **9**, 879 (1976) Helfand E., Wasserman Z. R., *Macromolecules*, **11**, 960(1978); Helfand E., Wasserman Z. R., *Macromolecules*, **13**, 994(1980).
Heller, P., *Rep. Prog. Phys*. **30**, 731 (1967).
Hill, T. L., ''Statistical Mechanics''. McGraw Hill, New York (1956).
Hu, Y. and Liu, H. L., *Fluid Phase Equilib*. **241**, 248 (2006).
Hu, Y., Lambert, S. M., Soane, D. S. and Prausnitz, J. M., *Macromolecules* **24**, 4356 (1991).
Hu, Y., Liu, H. L., Soane, D. S. and Prausnitz, J. M., *Fluid Phase Equilib* **67**, 65 (1991).
Hu, Y., Ying, X. G., Wu, D. T. and Prausnitz, J. M., *Fluid Phase Equilib* **83**, 289 (1992).
Hu, Y., Liu, H. L. and Prausnitz, J. M., *J. Chem. Phys*. **104**, 396 (1996).
Hu, Y., Liu, H. L. and Shi, Y. H., *Fluid Phase Equilib* **117**, 100 (1996).
Huang, Y. M., Jin, X. C., Liu, H. L. and Hu, Y., *Fluid Phase Equilib* **263**, 96 (2008).

Huggins, M. L., *J. Chem. Phys.* **9**, 440 (1941) Huggins M. L., *J. Phys. Chem.*, 46, 151(1942).
Janssen, R. H. C. and Nies, E., *Langmuir* **13**, 2784 (1997).
Jiang, J. W., Yan, Q. L., Liu, H. L. and Hu, Y., *Macromolecules* **30**, 8459 (1997).
Kellogg, G. J., Walton, D. G., Mayes, A. M., Lambooy, P., Russell, T. P., Gallagher, P. D. and et al. *Phys. Rev. Lett.* **76**, 2503 (1996).
Kierlik, E. and Rosinberg, M. L., *J. Chem. Phys.* **97**, 9222 (1992) Kierlik E., Rosinberg M. L., *J. Chem. Phys.*, 99, 3950(1993).
Kikuchi, R., *Phys. Rev.* **81**, 988 (1951) Kikuchi R., J. Chem. Phys., 47, 1664(1967).
Lacombe, R. H. and Sanchez, I. C., *J. Phys. Chem* **80**, 2568 (1976).
Lambert, S. M., Soane, D. S. and Prausnitz, J. M., *Fluid Phase Equilib* **83**, 59 (1993).
Lambooy, P., Russell, T. P., Kellogg, G. J., Mayes, A. M., Gallagher, P. D. and Satija, S. K., et al. *Macromolecules* **13**, 1602 (1980).
Li, H. and Huck, W. T. S., *Curr. Opin. Solid State Mater. Sci.* **6**, 3 (2002).
Li, W. and Wickham, R. A., *Macromolecules* **39**, 8492 (2006).
Li, W., Wickham, R. A. and Garbary, R. A., *Macromolecules* **39**, 806 (2006).
Li, J. L., He, H. H., Peng, C. J., Liu, H. L. and Hu, Y., *Fluid Phase Equilib* **276**, 57 (2009).
Li, J. L., He, H. H., Peng, C. J., Liu, H. L. and Hu, Y., *Fluid Phase Equilib.* **286**, 8 (2009).
Li, J. L., Tong, M., Peng, C. J., Liu, H. L. and Hu, Y., *Fluid Phase Equilib.* **287**, 50 (2009).
Likhtman, A. E. and Semenov, A. N., *Macromolecules* **27**, 3103 (1994).
Likhtman, A. E., Anastasiadis, S. H. and Semenov, A. N., *Macromolecules* **32**, 3474 (1999).
Liu, H. L. and Hu, Y., *Ind. Eng. Chem. Res.* **37**, 3058 (1998).
Liu, H. L., Yang, J. Y., Xin, Q. and Hu, Y., *Fluid Phase Equilib* **261**, 281 (2007).
Liu, H. L., Xu, H., Chen, H. Y., Peng, C. J. and Hu, Y., *Struct. Bonding* **131**, 109 (2008).
Ma, M., Krikorian, V., Yu, J. H., Thomas, E. L. and Rutledge, G. C., *Nano Lett.* **6**, 2969 (2006).
Madden, W. G., Pesci, A. I. and Freed, K. F., *Macromolecules* **23**, 1181 (1990).
Matsen, M. W. and Barrett, C., *J. Chem. Phys.* **109**, 4108 (1998).
Mita, K., Tanaka, H., Saijo, K., Takenaka, M. and Hashimoto, T., *Macromolecules* **41**, 6787 (2008).
Nemirovsky, A. M., Bawendi, M. G. and Freed, K. F., *J. Chem. Phys* **87**, 7272 (1987).
Nieswand, M., Dieterich, W. and Majhofer, A., *Phys. Rev. E* **47**, 718 (1993).
Oh, S. Y. and Bae, Y. C., *Eur. Polym. J.* **46**, 1328 (2010 a) Oh S. Y., Bae Y. C., *J. Phys. Chem. B*, 114, 8948(2010).
Ohta, T. and Kawasaki, K., *Macromolecules* **23**, 2413 (1990).
Ohta, T. and Kawasaki, K., *Macromolecules* **19**, 2621 (1986).
Ono S., and Kondo S. Molecular theory of surface tension in liquids, *in* ''Encyclopedia of Physics'' (S. Flügge, Ed.), Springer, Berlin (1960).
Oono, Y. and Puri, S., *Phys. Rev. A* **38**(434), 1542 (1988).
Oono, Y. and Shiwa, Y., *Modern Phys. Lett. B* **1**, 49 (1987).
Panagiotopoulos, A. Z. and Wong, V., *Macromolecules* **31**, 912 (1998).
Panayiotou, C., Pantoula, M., Stefanis, E., Tsivintzelis, I. and Economou, I. G., *Ind. Eng. Chem. Res.* **43**, 6952 (2004).
Pankavich, S., Shreif, Z., Miao, Y. and Ortoleva, P., *J. Chem. Phys.* **130**, 194115 (2009).
Park, M., Harrison, C., Chainkin, P. M., Register, R. A. and Adamson, D. H., *Science* **276**, 1401 (1997).
Patra, C. N. and Yethiraj, A., *J. Chem. Phys.* **112**, 1579 (2000) Patra C. N., Yethiraj A., *J. Chem. Phys.*, 118, 4702(2003).
Peng, C. J., Liu, H. L. and Hu, Y., *Chem. Eng. Sci.* **56**, 6967 (2001).
Peng, C. J., Liu, H. L. and Hu, Y., *Ind. Eng. Chem. Res* **41**, 862 (2002).
Peng, C. J., Liu, H. L. and Hu, Y., *Fluid Phase Equilib.* **206**(127), 147 (2003).
Pesci, A. I. and Freed, K. F., *J. Chem. Phys* **90**, 2017 (1989).
Prausnitz, J. M., Lichtenthaler, R. N. and de Azevedo, E. G., ''Molecular Thermodynamics of Fluid-Phase Equilibria, 3rd ed. Prentice Hall PTR (1999).

Prestipino, S. and Giaquinta, P. V., *J. Phys. Condens. Matter* **15**, 3931 (2003).
Reinhard, J., Dieterich, W., Maass, P. and Frisch, H. L., *Phys. Rev. E* **61**, 422 (2000).
Rider, D. A., Chen, J. I. L., Eloi, J. C., Arsenault, A. C., Russell, T. P., Ozin, G. A. and et al. *Macromolecules* **41**, 2250 (2008).
Rodriguez, A. L., Freire, J. and Horta, A., *J. Phys. Chem* **96**, 3954 (1992).
Sadus, R. J., ''Molecular simulation of fluids, theory, algorithms and object-orientation''. Amsterdam, Elsevier (1999).
Sanchez, I. C. and Lacombe, R. H., *J. Phys. Chem.* **80**, 2352 (1976) Sanchez I. C., Lacombe R. H., *Macromolecules*, 11, 1145(1978).
Scheutjens, J. M. H. M. and Fleer, G. J., *J. Phys. Chem.* **83**, 1619 (1979).
Scheutjens, J. M. H. M. and Fleer, G. J., *J. Phys. Chem.* **84**, 178 (1980).
Semenov, A. N., *Sov. Phys.-JEPT (Engl. Transl.)* **61**, 733 (1985).
Semenov, A. N., *Macromolecules* **22**, 2849 (1989).
Semenov, A. N., Bonet-Avalos, J., Johner, A. and Joanny, J. F., *Macromolecules* **29**, 2179 (1996).
Sengers J. V., and Sengers J. M. *in* ''Progress in Liquid Physica'' (C. A. Croxton, Ed.), Chapter 4. Wiley, New York (1978).
Sevink, G. J. A. and Zvelindovsky, A. V., *J. Chem. Phys.* **128**, 084901 (2008).
Sevink, G. J. A., Zvelindovsky, A. V., Fraaije, J. G. E. M. and Huinink, H. P., *J. Chem. Phys.* **115**, 8226 (2001).
Shin, M. S. and Kim, H., *Fluid Phase Equilib* **246**, 79 (2006).
Shin, K., Xiang, H., Moon, S. I., Kim, T., McCarthy, T. J. and Russell, T. P., et al. *J. Phys. Chem.* **57**, 584 (1953).
Song, K. X., Jia, Y. X., Sun, Z. Y. and An, L. J., *J. Chem. Phys.* **129**, 144901 (2008).
Stell, G. and Zhou, Y. Q., *J. Chem. Phys.* **91**, 3618 (1989).
Sun, Y., Steinhart, M., Zschech, D., Adhikari, R., Michler, G. H. and Gösele, U., et al. *Mol. Phys.* **41**, 85 (1980).
Tsivintzelis, I., Dritsas, G. S. and Panayiotou, C., *Ind. Eng. Chem. Res.* **45**, 7264 (2006).
Turner, M. S., *Phys. Rev. Lett.* **69**, 1788 (1992).
Walton, D. G., Kellogg, G. J., Mayes, A. M., Lambooy, P. and Russell, T. P., *Macromolecules* **27**, 6225 (1994).
Wang, Q., *J. Chem. Phys* **126**, 024903 (2007).
Wang, Q., Yan, Q. L., Nealey, P. F. and de Pablo, J. J., *J. Chem. Phys* **112**, 450 (2000).
Wang, Z., Li, B., Jin, Q., Ding, D. and Shi, A., *Macromol. Theory Simul* **17**, 86 (2008).
Wang, Z., Li, B., Jin, Q., Ding, D. and Shi, A., *Macromol. Theory Simul* **17**, 301 (2008).
Woodward, C. E., *J. Chem. Phys* **94**, 3183 (1991).
Wu, J. Z., *AIChE J.* **52**, 1169 (2006).
Xia, Y., Rogers, J. A., Paul, K. E. and Whitesides, G. M., *Chem. Rev.* **99**, 1823 (1999).
Xiang, H., Shin, K., Kim, T., Moon, S. I., McCarthy, T. J. and Russell, T. P., et al. *J. Polym. Sci. B: Polym. Phys.* **43**, 3377 (2005).
Xiang, H., Shin, K., Kim, T., Moon, S. I., McCarthy, T. J. and Russell, T. P., et al. *Macromolecules* **38**, 1055 (2005).
Xiao, X. Q., Huang, Y. M., Liu, H. L. and Hu, Y., *Macromol. Theory Simul.* **16**, 732 (2007).
Xin, Q., Peng, C. J., Liu, H. L. and Hu, Y., *Ind. Eng. Chem. Res* **47**, 9678 (2008).
Xin, Q., Peng, C. J., Liu, H. L. and Hu, Y., *Fluid Phase Equilib* **267**, 163 (2008).
Xin, Q., Xu, X. C., Huang, Y. M., Peng, C. J., Liu, H. L. and Hu, Y. *Sci. China B* **38**, 947 (2008).
Xu, H., Liu, H. L. and Hu, Y., *Macromol. Theory Simul.* **16**, 262 (2007).
Xu, H., Liu, H. L. and Hu, Y., *Chem. Eng. Sci.* **62**, 3494 (2007).
Xu, H., Wang, T. F., Huang, Y. M., Liu, H. L. and Hu, Y., *Ind. Eng. Chem. Res.* **47**, 6368 (2008).
Xu, X. C., Liu, H. L., Peng, C. J. and Hu, Y., *Fluid Phase Equilib.* **265**, 112 (2008).
Xu, X. C., Peng, C. J., Cao, G. P., Liu, H. L. and Hu, Y., *Ind. Eng. Chem. Res.* **48**, 7828 (2009).

Xu, X. C., Peng, C. J., Huang, Y. M., Liu, H. L. and Hu, Y., *Ind. Eng. Chem. Res.* **48**, 11189 (2009).
Yan, Q. L., Liu, H. L. and Hu, Y., *Macromolecules* **29**, 4066 (1996).
Yan, Q. L., Liu, H. L. and Hu, Y., *Fluid Phase Equilib* **218**, 157 (2004).
Yang, J. Y., Yan, Q. L., Liu, H. L. and Hu, Y., *Polymer* **47**, 5187 (2006).
Yang, J. Y., Peng, C. J., Liu, H. L., Hu, Y. and Jiang, J. W., *Fluid Phase Equilib* **244**, 188 (2006).
Yang, J. Y., Xin, Q., Sun, L., Liu, H. L., Hu, Y. and Jiang, J. W., et al. *Fluid Phase Equilib*. **249**, 192 (2006).
Yang, J. Y., Peng, C. J., Liu, H. L. and Hu, Y., *Ind. Eng. Chem. Res* **45**, 6811 (2006).
Ye, Z. C., Cai, J., Liu, H. L. and Hu, Y., *J. Chem. Phys*. **123**, 194902 (2005).
Ye, Z. C., Chen, H. Y., Cai, J., Liu, H. L. and Hu, Y., *J. Chem. Phys*. **125**, 124705 (2006).
Ye, Z. C., Chen, H. Y., Liu, H. L., Hu, Y. and Jiang, J. W., *J. Chem. Phys*. **126**, 134903 (2007).
Yethiraj, A. and Woodward, C. E., *J. Chem. Phys* **102**, 5499 (1995).
Yin, Y., Sun, P., Chen, T., Li, B., Jin, Q., Ding, D. and et al. *Chem Phys Chem* **5**, 540 (2004).
Yu, Y. X. and Wu, J. Z., *J. Chem. Phys.* **117**, 2368 (2002).
Yu, B., Sun, P., Chen, T., Jin, Q., Ding, D. and Li, B., et al. *J. Chem. Phys* **126**, 204903 (2007).
Yu, B., Sun, P., Chen, T., Jin, Q., Ding, D., Li, B. and et al. *J. Chem. Phys* **127**, 114906 (2007).
Yu, B., Li, B., Jin, Q., Ding, D. and Shi, A., *Macromolecules* **40**, 9133 (2007).
Zhang, S. L., Cai, J., Liu, H. L. and Hu, Y., *Mol. Simul*. **30**, 143 (2004).
Zheng, W. and Wang, Z. G., *Macromolecules* **28**, 7215 (1995).
Zhi, D. Y., Huang, Y. M., Han, X., Liu, H. L. and Hu, Y., *Chem. Eng. Sci.* **65**, 3223 (2010).
Zhou, Y. Q. and Stell, G., *J. Chem. Phys*. **96**(1504), 1507 (1992).
Zhou, S. Q. and Zhang, X. Q., *Phys. Rev. E* **64**, 011112 (2001).
Zhu, Y. and Jiang, W., *Macromolecules* **40**, 2872 (2007).